TOPICAL REVIEW

Magnetic-decoration imaging of structural transitions induced in vortex matter

Yanina Fasano[1,3] **and Mariela Menghini**[2]

[1] Département de Physique de la Matière Condensée, Université de Genève, Geneva, Switzerland

[2] INPAC-Institute for Nanoscale Physics and Chemistry, Nanoscale Superconductivity and Magnetism and Pulsed Fields Group, Katholieke Universiteit Leuven, Leuven, Belgium

E-mail: yanina.fasano@physics.unige.ch

Abstract

During the last two decades, vortex structural transitions in type-II superconductors have been the subject of a considerable amount of theoretical and experimental studies. This article presents an exhaustive review of reports on real-space imaging of vortex structural transitions induced by introduced pinning potentials. The focus is set on the application of the magnetic-decoration technique to image structural transformations in three-dimensional vortex matter. Technical details, open issues and selected results in the paradigmatic high- and low-T_c materials $Bi_2Sr_2CaCu_2O_8$ and $NbSe_2$ are presented. The role played by substrate disorder, nucleation and growth dynamics of the vortex solid, elastic properties and anisotropy of vortex matter is analysed.

(Some figures in this article are in colour only in the electronic version)

1. Introduction

The study of the statics and dynamics of vortex matter in type-II superconductors remains an active field of research [1]. The ability to control the vortex lattice constant and elastic properties over a wide range of values, the availability of a large number of imaging, transport, and thermodynamic probes, and the plethora of available systems and regimes, have contributed to a prolific collaboration between theory and experiment that continues to increase the understanding in this area. In particular, vortex structural transitions have received considerable attention.

These transformations can be induced by tuning the magnetic field that modifies the balance between the vortex–vortex and vortex–substrate interaction energies. The latter strongly depends on the spatial distribution of the 'substrate' quenched disorder, i.e. on the pinning potential landscape of the superconducting sample [1]. For the case of magnetic superconductors the coupling of superconductivity with magnetism also affects the vortex–substrate interaction,

leading to structural transitions as a function of magnetic field [2, 3]. Furthermore, structural transitions in the vortex structure can be induced at will by engineering suitable pinning centres.

The elastic properties and dimensionality of vortex matter strongly influence the statics and dynamics of these transformations. For instance, the two-dimensional vortex matter nucleated in thin films is a longitudinally rigid structure, and structural transitions induced at the sample surface propagate over the whole length of vortices. In contrast, three-dimensional vortex matter nucleated in crystals is laterally and longitudinally elastic, and therefore transformations induced at the surface propagate into the interior over a distance that can be smaller than the sample thickness. The anisotropy of the superconducting properties strongly affects the vortex structure (VS) elastic moduli [1] and therefore influences the propagation of induced symmetry transitions. The nucleation and growth dynamics of the vortex solid also plays a determinant role.

In order to study these structural transitions, direct imaging of individual vortices is crucial. In particular, the

---

[3] Author to whom any correspondence should be addressed.

magnetic-decoration technique [4] provides snapshots of the VS with single-vortex resolution in macroscopic fields of view. This imaging method has a long and venerable history in vortex matter. It consists in the evaporation of nanosized magnetic particles that are attracted towards vortices due to the magnetic force generated by the gradient of local magnetic induction. Therefore, the particles land on the surface of the sample, *decorating* vortex positions.

This article reviews recent investigations and open issues in magnetic-decoration imaging of structural transitions induced in vortex matter. Section 2 presents an overview on the elastic properties and different phases of vortex matter relevant to the understanding of the experimental results described in the manuscript. Section 3 is a review of the different experiments on direct imaging of vortex structural transitions induced by means of introduced pinning potentials. Results obtained in two- and three-dimensional vortex matter using the magnetic-decoration and other techniques are presented. Then in section 4 the focus is set on the technical details of the magnetic-decoration imaging of such vortex structural transitions. The section starts with a brief introduction to the different vortex-imaging techniques, includes a detailed description of the magnetic-decoration working principle (section 4.1) and a discussion of the state of the art and challenges of this technique (section 4.2). Sections 5 and 6 turn the attention of the reader to two examples of structural transitions induced in three-dimensional vortex matter and imaged by means of magnetic decoration. The case of the symmetry transition induced in the layered and high-T_c $Bi_2Sr_2CaCu_2O_8$ superconductor is discussed in section 5, whereas section 6 presents results in the moderately anisotropic and low-T_c $NbSe_2$ system. The structural transitions induced by the same type of engineered pinning potentials are dissimilar for both materials. This is analysed considering the effect of elastic properties, anisotropy and nucleation and growth dynamics of the vortex solid. These two cases have been chosen in order to illustrate the richness of vortex-structural-transition phenomena accessible when combining magnetic-decoration imaging and engineering of pinning potentials in different materials.

2. Elastic properties and different phases of vortex matter

In order to study the effect of introduced pinning, a discussion on the structural properties of vortex matter nucleated in samples with naturally present bulk pinning becomes necessary. The response of the vortex structure to perturbations generated by either natural or introduced pinning potentials can be described within an elastic theory [1]. The structural properties of vortex matter depend on the balance between thermal, pinning and vortex-interaction energies [1], i.e. on the particular superconducting material that constitutes the VS substrate. Therefore, a discussion on the elastic properties and the variety of vortex phases stabilized in different systems is fundamental to understanding the physics of vortex structural transitions induced by engineered pinning potentials.

2.1. Elastic properties of vortex matter

The elastic properties of vortex matter depend on the superconducting penetration depth λ and coherence length ξ, as well as on the material anisotropy $\gamma \sim \lambda_c/\lambda_{ab} \sim \xi_{ab}/\xi_c$ [1]. Here $\lambda_{ab,c}$ and $\xi_{ab,c}$ are the penetration depths and coherence lengths for supercurrents running perpendicular (ab) and parallel (c) to the anisotropy axis. The elastic matrix of the vortex structure has three independent moduli for compression (c_{11}), tilt (c_{44}) and shear (c_{66}) deformations [1]. The elastic moduli have their origin in the repulsive interaction between the supercurrents of vortices. For two vortices in the London limit ($\kappa = \lambda/\xi \gg 1$) [5] the repulsive interaction reads

$$E_{12}^{int} = \frac{\Phi_0^2}{8\pi^2\lambda^2} K_0\left(\frac{r_{12}}{\lambda}\right) = 2\epsilon_0 K_0\left(\frac{r_{12}}{\lambda}\right) \qquad (1)$$

per unit length. The distance between vortices is r_{12}, K_0 is the zeroth-order Hankel function and $\epsilon_0 = (\Phi_0/4\pi\lambda)^2$ is the energy scale per unit length [5]. The vortex–vortex interaction energy increases with field and rapidly vanishes at $t = T/T_c \sim 1$ as a consequence of the divergence of $\lambda(t) \approx \lambda(0)/(1-t^4)^{1/2}$ [5]. This interaction energy is at the basis of a vortex elastic theory that describes the temperature and magnetic field evolution of the elastic moduli neglecting the effect of thermal fluctuations [1].

Experimentally, one clever attempt to estimate the value of the elastic moduli was to perform a magnetic decoration of vortices entering and leaving the superconducting crystal on opposite surfaces (two-sided decoration) [6–8]. The idea is that by correlating the positions of individual vortices when emerging from the opposite surfaces, information on the wandering of vortices inside the sample can be obtained [9, 10]. The dependence of this wandering on the elastic moduli of the vortex structure [10] allowed the estimation of c_{11}, c_{44} and c_{66} for the low- and high-T_c materials $NbSe_2$ [8] and $Bi_2Sr_2CaCu_2O_8$ [6, 7]. The measured value of the tilt modulus is in agreement with the theoretical estimation [7] and is found to be three ($Bi_2Sr_2CaCu_2O_8$) [6, 7] to two ($NbSe_2$) [8] orders of magnitude greater than the measured shear and compression modulus. Furthermore, the ratios c_{44}/c_{11} and c_{44}/c_{66} are found to be three orders of magnitude higher than predicted by the elastic theory that neglects thermal fluctuations [6–8]. In the case of two-sided decorations in $Bi_2Sr_2CaCu_2O_8$ this was interpreted as the effect of the thermal fluctuations not considered in the theory [7]. Regarding the experiments in $NbSe_2$, it was suggested that the evaluation of these ratios is affected by the presence of topological defects in the VS decorated at low temperatures, after a field-cooling process [8]. Regardless of the origin of this downward renormalization of c_{11} and c_{66}, these results indicate that the magnitude of c_{44} is reasonably estimated by the elastic theory that neglects thermal fluctuations [1].

The elastic response of vortex matter to introduced pinning structures is dramatically sensitive to the anisotropy of the superconducting properties [1]. For moderately anisotropic materials, where the coherence length ξ_c is greater than the spacing between superconducting planes, the order parameter is continuous along the c axis and vortices can be described with an anisotropic Ginzburg–Landau theory [11]. An example

of these materials is the low-T_c NbSe$_2$ with $\gamma^2 \sim 11$ [12]. When the anisotropy is extremely high, as in the case of Bi$_2$Sr$_2$CaCu$_2$O$_8$ ($\gamma^2 \sim 2\,10^4$ [1]), ξ_c becomes smaller than the spacing between the superconducting CuO$_2$ planes [1]. The superconducting order parameter is therefore discontinuous along the c direction: it is finite in the CuO$_2$ layers and vanishes in between [13]. In this case the VS is constituted of stacks of pancake vortices (PVs) located in the superconducting planes and coupled from layer to layer through electromagnetic and Josephson interactions [1]. This coupling weakens at high temperatures, close to the melting line, where pancake vortices become decoupled and vortices behave as quasi-two-dimensional entities [1, 14, 15].

The effect of the superconducting anisotropy of the material on induced structural transitions can be analysed by considering the dependence of c_{44} (roughly three orders of magnitude larger than c_{11} and c_{66} [6–8]) on γ. In the particular case of experiments at a fixed vortex density equal to that of pinning sites, such as those described in sections 5 and 6, the elastic response of the VS is mainly governed by the tilting modulus. Since $c_{44}(\vec{k}) = c_{44}(k_\perp, k_z)$ ($\vec{k_\perp} = (k_x, k_y)$) is dispersive, the propagation of structural transitions depend on the wavelength of the perturbation. In particular, the VS softens for short wavelengths, as deduced from the evolution of the two components of c_{44} with $\vec{k}$ [1],

$$c_{44}(\vec{k}) = c_{44}^{\text{latt}}(\vec{k}) + c_{44}^{\text{iv}}(\vec{k}). \tag{2}$$

Here the first term is associated with the vortex–vortex interaction and the second comes from the response of individual vortices to longitudinal perturbations (k_z). The lattice term is sensitive to longitudinal as well as transversal ($k_\perp$) perturbations [1],

$$c_{44}^{\text{latt}}(k_\perp, k_z) = \left(\frac{B^2}{4\pi}\right) \frac{1}{1 + (\gamma\lambda)^2 k_\perp^2 + \lambda^2 k_z^2}. \tag{3}$$

In the magnetic field region $B < \Phi_0/\lambda^2$ ($\sim$500 G for Bi$_2$Sr$_2$CaCu$_2$O$_8$), and neglecting the effect of thermal fluctuations, the individual-vortex contribution for layered materials takes the form [1]

$$c_{44}^{\text{iv}}(k_z) = \frac{B^2}{8\pi\lambda^2 k_{\text{BZ}}^2}\left[\gamma^{-2}\ln\left(\frac{(\kappa\gamma)^2}{1 + (\lambda\gamma)^2 k_{\text{BZ}}^2 + \lambda^2 k_z^2}\right)\right.$$
$$\left. + \frac{1}{(\lambda k_z)^2}\ln\left(1 + \frac{\lambda^2 k_z^2}{1 + \lambda^2 k_{\text{BZ}}^2}\right)\right]. \tag{4}$$

The Brillouin momentum $k_{\text{BZ}} = \sqrt{4\pi B/\Phi_0}$ is that of a two-dimensional hexagonal VS with the lattice parameter determined by B. The first logarithmic term in $c_{44}^{\text{iv}}(k_z)$ is associated with the Josephson coupling [16] between adjacent superconducting layers, while the second has origin in the electromagnetic coupling [1]. The latter has to be considered only in the case of extremely layered materials such as Bi$_2$Sr$_2$CaCu$_2$O$_8$ [1].

Figure 1 presents the evolution of $c_{44}(k_\perp, k_z)$ with the wavelength of the longitudinal perturbation ($2\pi/k_z$) for the two paradigmatic high- and low-T_c materials Bi$_2$Sr$_2$CaCu$_2$O$_8$ and NbSe$_2$. It is worth mentioning that both materials have
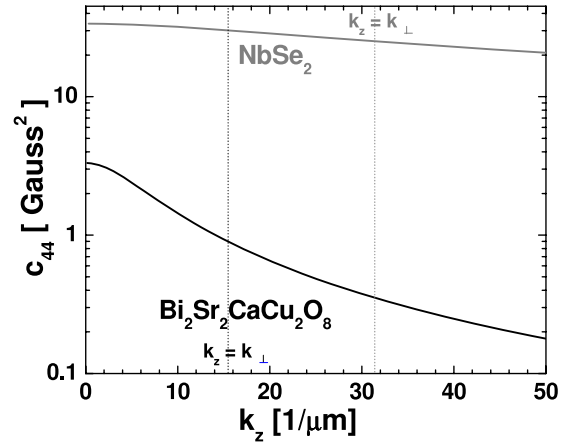
Figure 1. Tilting modulus $c_{44}(k_\perp, k_z)$ as a function of the wavelength of the longitudinal perturbation, k_z, for Bi$_2$Sr$_2$CaCu$_2$O$_8$ at $T_i \sim T_m$ ($\lambda(T_i) = 0.4$ μm; see section 5 for details) and NbSe$_2$ at $T = 4.2$ K ($\lambda(4.2\text{ K}) = 0.2$ μm). In both cases $B = 37.4$ G ($a = 0.8$ μm) and the wavelength of the perpendicular perturbation $k_\perp = 1/\lambda$.

$\lambda(0) \sim 2000$ Å [1, 12]. However, in order to motivate the discussions of sections 5 and 6, in figure 1 c_{44} is calculated at different temperatures for each material (see the caption of figure 1). Nevertheless, the three orders of magnitude difference in γ is responsible for the Bi$_2$Sr$_2$CaCu$_2$O$_8$ vortex structure being roughly one order of magnitude softer than that of NbSe$_2$. As will be discussed in sections 5 and 6, this is at the origin of the different structural transitions induced in both materials by equivalent introduced pinning structures.

2.2. Vortex phases in high- and low-T_c superconductors

In ideal superconducting samples, free of crystal defects, the ground-state VS is the hexagonal Abrikosov lattice [17]. The lattice parameter of this elastic structure is tuned by the average magnetic induction, $a = 1.075\sqrt{\Phi_0/B}$, where $\Phi_0 = hc/2e = 2.07 \times 10^{-7}$ G cm^2 is the flux quantum [1].

Real samples, even top-quality ones, present a density of atomic defects orders of magnitude larger than that of vortices, resulting in a dense distribution of point-like pinning centres. This type of quenched disorder, even if arbitrarily weak, destroys the translational long-range order of the Abrikosov crystal [18]. It was theoretically proposed [19–21] and experimentally supported [22–25] that the phase stable at low fields and temperatures is the Bragg glass. This phase presents long-range orientational and quasi-long-range positional correlation, a structure factor with algebraically divergent Bragg peaks and a glass-like dynamic response [26]. It has been proposed that this vortex phase lacks topological defects at zero temperature [20, 21, 27, 28]. If thermal or quenched disorder are substantially increased the nearly ordered Bragg glass becomes unstable [26].

In particular, high-T_c superconductors present a liquid vortex phase [29–33] that solidifies into the low-field Bragg glass through a first-order phase transition at a temperature $T_m(H)$ (or field $H_m(T)$) [32–34]. Increasing the magnetic field produces a relative enhancement of the vortex structure-quenched disorder interaction with respect to the vortex–vortex interaction energy [26]. As a consequence, on
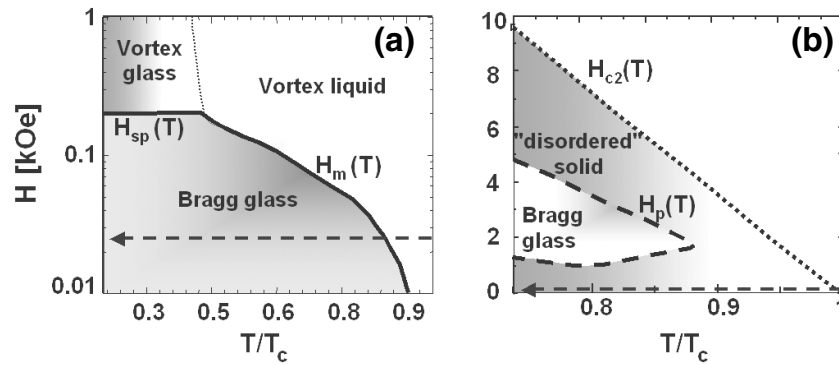
Figure 2. Vortex phase diagrams in reduced temperature for high- and low-T_c materials: (a) optimally doped $Bi_2Sr_2CaCu_2O_8$ with $T_c = 90$ K (data taken from [41]) and (b) Fe-doped $NbSe_2$ with $T_c = 5.7$ K (data taken from [42]). The high critical field, $H_{c2}(T)$, melting, $H_m(T)$, peak effect, $H_p(T)$ and second peak, $H_{sp}(T)$, lines are indicated. First- and second-order phase transitions are depicted with solid and dotted lines, respectively. The dashed arrows indicate the paths typically followed when performing field-cooling magnetic-decoration experiments.

increasing magnetic field the Bragg glass transforms into a topologically disordered vortex glass [35] through a first-order phase transition (second-peak line, H_{sp}) [36–39]. In contrast, the vortex liquid transforms continuously into the vortex glass when cooling at high fields [40]. As an example, figure 2(a) presents the different vortex phases of pristine samples of $Bi_2Sr_2CaCu_2O_8$ [41] (the compound studied in section 5). The structural properties of the Bragg glass phase can be revealed by magnetic-decoration experiments performed at low temperatures after following a field-cooling path [23, 25] like the one schematically indicated in figure 2.

In the case of low-T_c materials, the vortex phase diagram mainly differs from that of high-T_c materials in that the vortex liquid phase is confined to fields close to the upper critical field H_{c2}, or is entirely absent. This is illustrated in figure 2(b), which shows the vortex phases of Fe-doped $NbSe_2$ ($T_c = 5.7$ K) [42]. In low-T_c materials the peak in critical current detected at a field $H_p(T)$ was associated with a transition between the Bragg glass ($H < H_p(T)$) and the so-called disordered vortex solid [26, 43]. From the interpretation of some transport [42–44] and neutron diffraction [45] results on $NbSe_2$ and Nb, respectively, it was proposed that the phase stable at fields $H > H_p$ is topologically disordered. However, real-space imaging of the VS by means of the magnetic-decoration technique allowed us to directly observe that the structure of the so-called disordered phase is polycrystalline rather than amorphous [46, 47]. These results stressed that the relation between transport and structural properties of vortex matter is not trivial: critical currents are determined by vortex displacements on lengthscales of the order of ξ, whereas at low fields the topology of the VS is determined by much larger vortex displacements, of the order of $a \gg \xi$ [26, 46, 47].

In some materials, the natural presence of correlated pinning potentials produces the stabilization of more exotic vortex phases. For example, in $YBa_2Cu_3O_7$ samples the correlated pinning generated by twin boundaries stabilizes a low-field phase where vortices are localized at the defects, the Bose glass [48–50]. Furthermore, as will be discussed in this manuscript, introduced pinning potentials can be used to induce vortex structural transitions, which increases the complexity of the vortex phase diagram.

3. Imaging vortex structural transitions induced by engineered pinning potentials

A wealth of works report on static and dynamic properties of structural transitions induced in vortex matter by means of pinning potentials introduced either on the surface or in the bulk of the samples. This section presents an exhaustive overview of the literature in this area. The results are described in two sections: section 3.1 presents experiments in two-dimensional vortex matter, whereas in section 3.2 data obtained in three-dimensional vortex structures are discussed. Our work presented in sections 5 and 6 contributes in particular to the latter case.

3.1. Experiments in two-dimensional vortex matter

The last decades have witnessed a comprehensive investigation of the dynamical matching of two-dimensional vortex matter with periodic arrays of film-thickness modulations [51], dots (magnetic [52–56] or non-magnetic [52]), holes [57–61], superconducting wire networks [62, 63] and irradiation-induced defects [64]. This was the consequence of the booming development of an engineering of pinning centres with dimensions of the order of the typical coherence length of conventional superconductors, $\xi \sim 100$ nm. These technical advancements were triggered by the progress on nanofabrication methods. Some of these methods are based on electron beam, x-ray and scanning probe lithography, focused ion beam, step growth, irradiation-induced damage of the samples, self-assembled structures and nanotemplates [65].

The dynamical matching effect is detected as an increase of critical current for vortex densities commensurate with that of pinning centres, i.e. $n_v = B/\Phi_0 = m \cdot n_p$, where n_v and n_p are the number of vortices and pinning centres per unit area and m is a rational number. The fields B_Φ that fulfil the last relation with m an integer number are named matching fields, $B_1 = n_p \cdot \Phi_0$ being the first matching field. Theoretical simulations [66, 67] predict a variety of dynamical phases when tuning n_v/n_p. Experimentally, the phenomenon was studied for different geometries of pinning
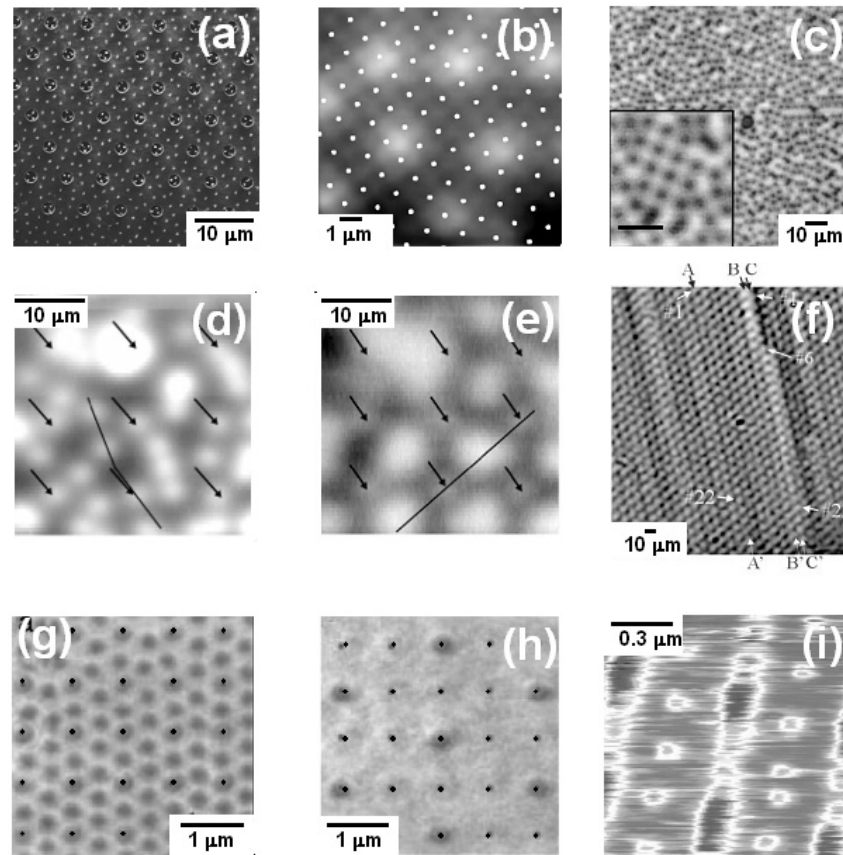
Figure 3. Examples of direct imaging of structural transitions induced in vortex matter. (a) Vortices (bright spots) trapped inside blindholes milled in a Nb film. Magnetic-decoration image taken at 4.2 K after field cooling (FC) the sample at 6.37 Oe. Reprinted with permission from [77]. Copyright (1996) by the American Physical Society. (b) Vortex (bright spots) configuration in a Pb film with a square array of Co/Pt dots (small white dots) observed by scanning Hall probe microscopy at 6.8 K after a FC at 1.6 Oe (1 vortex per $\approx$13 dots). Reprinted with permission from [85]. Copyright (2003) by the American Physical Society. (c) Vortex (dark spots) distribution in a Nb film with a square array of holes as revealed by scanning Hall probe microscopy at 3 K after a FC at 1.18 Oe (1 vortex per 5 holes). Reprinted with permission from [86]. Copyright (2002) by the American Physical Society. (d) Vortex configuration (bright spots) in an Al film with a square array of holes (indicated by the arrows) as seen by scanning SQUID microscopy at 1.14 G (5 vortices per hole) at $T/T_c = 0.32$ and (e) 0.96. Reprinted with permission from [91]. Copyright (2004) by the American Physical Society. (f) Multiple-quanta vortices (bright spots) trapped by a triangular array of holes forming commensurate (AA') and incommensurate (BB' and CC') channels in an YBa$_2$Cu$_3$O$_{7-\delta}$ film. Image obtained by high-resolution magneto-optics at 8 K and 370 Oe. Reprinted with permission from [84]. (g) Vortex configuration (dark spots) in a Nb film with a square array of crystal defects produced by ionic irradiation (small black dots) imaged by Lorentz microscopy after zero-field cooling up to a vortex density of 4 vortices per defect. From [76]. Reprinted with permission from AAAS. (h) Same experiment with the vortex density reduced to 1 vortex per 4 defects. From [76]. Reprinted with permission from AAAS. (i) Scanning tunnelling microscopy image of vortices (small circular features) nucleated in a NbSe$_2$ crystal patterned with a square array of gold dots (dark elliptical features with 6 flux quanta each) obtained at 4.2 K and 825 G. Reprinted with permission from [92]. Copyright (2004) by the American Physical Society.

structures [55, 60, 68–72], mainly by magnetization [70, 73] and transport [53–55, 61, 68] measurements.

Several works report on direct imaging of pinning-induced vortex structural transitions [25, 62–64, 74–93]. The static and dynamic properties of these transformations have been visualized with single-vortex resolution in the range of vortex spacings between 10 and ~1000 nm (magnetic fields between 10 000 and ~0 G). The following paragraphs present a complete description of the results obtained in these experiments, pictorially summarized in figure 3.

The first reports [62, 63] present scanning Hall probe microscopy (SHPM) and magnetic-decoration images of the vortex configuration nucleated in a superconducting wire network. In both cases the samples are square grids of Nb wires with lattice parameters $a \sim 1$–2 μm, nearly four times the width of the wires. The geometry of the samples constitutes a square pinning potential for the vortex structure. In the SHPM experiments [62] the local magnetic field was mapped as a function of flux per unit cell, or filling factor, over areas of typically 20×20 μm^2. For a field corresponding to one vortex every two unit cells the checkerboard ground state is observed, and on reducing the magnetic field, vacancies in this structure are detected [62]. Correlated vortex hopping when warming the sample close to the critical temperature is also reported [62]. In the magnetic-decoration experiments the field was kept fixed and several networks with different lattice parameters (different filling factors) were simultaneously decorated [63]. The checkerboard structure was also observed close to 1/2 filling factor as well as other ordered structures at different fractional
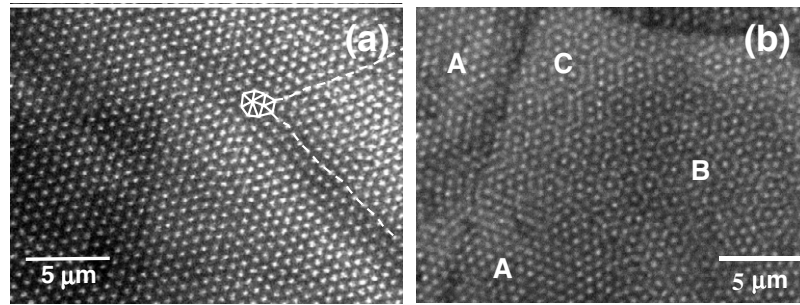
Figure 4. Effect of Bitter pinning for the first matching field. (a) Matching between the $Bi_2Sr_2CaCu_2O_8$ vortex matter and the Bitter pinning. Reprinted with permission from [81]. Copyright (2000) by the American Physical Society. The topological defects of the pinning structure, such as the highlighted edge dislocation, are all reproduced by the VS. (b) Partial matching between the $NbSe_2$ vortex matter and the Bitter pinning. Reprinted with permission from [78], copyright 1999 by the APS. In region A the VS matches the Bitter pinning whereas in regions B and C both structures are misaligned by 30° and 40°, respectively, forming Moiré patterns. In both cases the magnetic decorations were performed at 4.2 K after field cooling at 36 Oe.

filling factors [63]. For non-fractional filling factors, defects and domain walls on the ordered structures were detected. For a given filling factor, the spatial distribution of these defects differs from one sample to another [63].

Afterwards, the electron beam lithography technique, eventually combined with different material-deposition methods, was extensively applied to engineer pinning structures in superconducting films. The first study that directly observed vortex structural transformations in this case applied the magnetic-decoration technique to image vortices trapped inside blindholes (holes with bottom) in a 1700 Å thick Nb film [77]; see figure 3(a). The blindholes (1500 Å deep) were generated using a combination of lithographic and reactive-ion etching techniques. The number of vortices trapped in each pinning site was measured as a function of magnetic field and depth of the blindholes. This magnitude is found to be independent of the bottom thickness, in agreement with theoretical calculations [77].

Scanning Hall probe and scanning SQUID microscopies were recently employed to visualize vortex structural transitions induced by magnetic dots [80, 82, 85, 87] and holes [86, 91] introduced in films; see for example figures 3(b)–(e). In these studies individual vortices are resolved up to only few gauss.

Magnetic pinning structures consisting of square arrays of single-domain dots magnetized in-plane [80, 82] or out-of-plane [83, 85, 87] were generated in Pb films. Scanning Hall probe images reveal that, for example, in the case of in-plane magnetized dots [80, 82] and at a field B_1 vortices are pinned at the position where the dot stray-field points in the opposite direction to the applied field. On increasing the magnetic field, no interstitial vortices are observed up to B_2 and therefore a square multi-quanta vortex lattice is stabilized.

In the case of pinning structures generated by holes, the first reported study [86] applies scanning Hall probe microscopy to image the vortex configuration at a fixed temperature (3 K). In this experiment a square array of holes was milled in a Nb film. Vortices are found to be located in the holes up to fields corresponding to $m = 2$ [86]. However, for $m = 3$ the flux images become blurred, making it impossible to discern the vortex configuration. The authors claim this is due

to an abrupt appearance of interstitial vortices [86]. Therefore, in this case the saturation number of the holes with radius R_D, $n_s \sim R_D/2\xi(T) \sim 2$ ($T/T_c = 0.35$). At fractional multiples of B_1, domains of well-ordered vortices are separated by a network of domain boundaries [86].

More recently, the vortex spatial distribution in the presence of a square array of holes was observed as a function of temperature by means of scanning SQUID microscopy [91]. The study was performed on an Al film with a thickness (170 nm) such that it exhibits a type-II behaviour [91]. When field cooling at a magnetic field corresponding to $m = 5$ ($B = 1.14$ G) every hole traps one flux quantum and the remaining vortices are located at interstitial positions. The difference in the n_s measured in this experiment and that of Nb films [82, 86] arises from the larger ratio $\xi(T)/R_D$. The configuration of interstitial vortices varies with temperature. At low temperatures ($T/T_c = 0.32$), λ and ξ are smaller than the square array period (1 μm), and interstitial vortices are located at random; see figure 3(d). At higher temperatures ($T/T_c = 0.96$) the superconducting parameters increase up to an appreciable fraction of the array period, interstitial vortices become sensitive to the periodic pinning and therefore they are mainly located at the centre of the square cell, as shown in figure 3(e).

The dynamics of vortex penetration in $YBa_2Cu_3O_{7-\delta}$ films with triangular arrays of holes has been observed with high-resolution magneto-optics [84], as reproduced in figure 3(f). Although in this experiment individual vortices were not resolved, information on single-vortex penetration was obtained. When increasing the field after a zero-field cooling, vortices penetrate and occupy holes up to a saturation number of $280 \sim R_D/2\xi(T)$ per pinning site. On further increasing the field, incommensurate channels form along the rows of pinning sites, with vortices eventually hopping between channels. Results from numerical simulations [94] are in agreement with these observations. The discrepancy between the saturation number measured in this experiment [84] and in the ones previously described [82, 86] comes from the difference in the coherence length of the materials (more than one order of magnitude smaller for $YBa_2Cu_3O_{7-\delta}$ than for Nb, Al and Pb) and the particular values
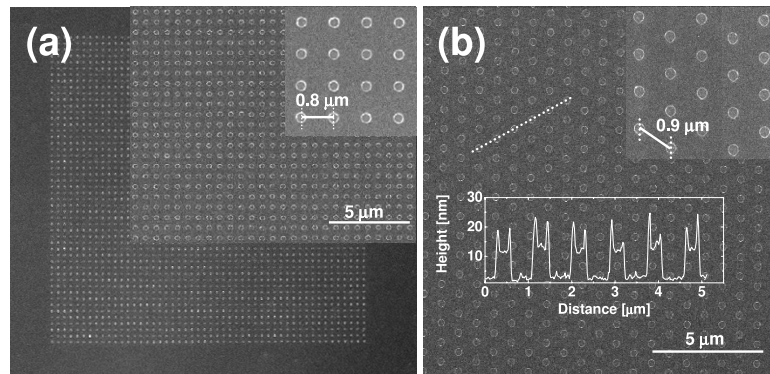
Figure 5. Scanning electron microscopy images of (a) square and (b) hexagonal arrays of Fe dots used as pinning structures in $Bi_2Sr_2CaCu_2O_8$ and $NbSe_2$ samples. Inset: Height profile measured along the dotted line of the main panel by means of atomic force microscopy.

of R_D (2 μm [84] versus 0.3–0.5 μm [82, 86]). Recently, magneto-optic experiments with similar flux resolution have imaged the dynamics of vortex penetration in $YBa_2Cu_3O_{7-\delta}$ films patterned with a ratchet pinning structure [95].

Another method to create a controlled distribution of pinning sites is the generation of localized crystal defects by irradiating the sample with a focused ion beam. The interaction of the vortex structure with square arrays of defects was studied with Lorentz microscopy in Nb films [64, 76, 96]. In the case of a square array of defects, snapshots taken during ramping-field experiments reveal that vortices form regular lattices with dissimilar symmetries for different matching conditions. For example, for $B_{1/4}$, vortices are located on defects forming a distorted hexagonal structure; see figure 3(h). While for B_1 all vortices occupy defects replicating their square structure, for B_4 the vortex structure is hexagonal with 1/4 of vortices occupying defects and the rest at interstitial positions; see figure 3(g) [64]. Real-time flux-penetration images show that on increasing the field up to B_1, vortices are located only in the defects, progressively from the edge towards the centre of the sample. On further increasing the field, vortices occupy interstitial sites. The difference with the saturation number found in other experiments in low-T_c materials [82, 86] arises from the dimensions of the pinning sites (smaller in this case).

3.2. Experiments in three-dimensional vortex matter

In the case of three-dimensional vortex matter a richness of phenomena associated with structural transitions is expected because the structure is softer than that nucleated in films. Nevertheless, the number of studies that focus on vortex structural transitions induced in crystals is not so prominent [25, 74, 75, 78, 79, 81, 88–90, 92, 93]. In the following paragraphs, the few works available in the literature are discussed.

Seminal works studied the effect of a random distribution of columnar defects by means of the magnetic-decoration technique [74, 75]. Columnar defects that extend along the whole sample thickness and that are randomly distributed in the plane are generally created by irradiation with heavy ions [97]. The first report [74] studied the vortex structural

transition induced in $Bi_2Sr_2CaCu_2O_8$ samples by a distribution of columnar defects with a density approximately two orders of magnitude larger than that of vortices. Irradiating only a part of the sample allowed the observation that the columnar defect distribution destroys the hexagonal translational order of the VS nucleated in pristine regions. In the same material, a later work [75] combined magnetic decoration and chemical etching to directly observe the vortex and columnar defects location in fully irradiated samples. The occupancy of columnar defects by vortices, the origin of the observed topological defects and the characteristic translational and orientational order of the vortex structure were studied in samples with densities of vortices roughly five times greater and four times smaller than that of columnar defects [75]. More recent studies [88] in irradiated $Bi_2Sr_2CaCu_2O_8$ crystals with different densities of columnar defects reveal that polycrystalline or amorphous vortex structures are induced, depending on the relative density of vortices and columnar defects. In spite of the relevance of these results, the inability in controlling the spatial distribution of columnar defects limits its application to induce vortex symmetry transitions.

In a more controllable way, arrays of magnetic pinning sites generated on the sample surface were used to induce structural transitions in three-dimensional vortex matter [25, 78, 79, 81, 89, 90]. In particular, the quasi-periodic Bitter pinning [78, 79, 81] is generated by the Fe agglomerates remaining from a first magnetic decoration of the vortex structure. The Bitter pinning was successfully applied to pin vortices at the surface of $Bi_2Sr_2CaCu_2O_8$ crystals for the first matching field [25]; see figure 4. This pinning breaks the translational symmetry of the vortex system preserving the quasi-long-range order characteristic of the Bragg glass. In the case of the low-T_c superconductor $NbSe_2$, the Bitter pattern presents a polycrystalline structure [78, 79, 81]. For the first matching field, only 30% of vortices match pinning sites whereas the rest form Moiré patterns associated with a local misalignment between the vortex and pinning structures. The dissimilar vortex response in $Bi_2Sr_2CaCu_2O_8$ and $NbSe_2$ is a consequence of the different mechanisms of nucleation and growth of the vortex solid in both materials [81]. This work triggered molecular-dynamics simulation studies of the

vortex structure–Bitter pinning matching conditions when bulk disorder is non-negligible [98].

Structural transitions in three-dimensional vortex matter have also been induced by means of a more versatile method: arrays of magnetic dots with controlled symmetry and size deposited on the surface of superconducting crystals [25, 89, 90, 99–101]. These structures were obtained by positive lift-off of patterns engraved on a resin by means of electron beam lithography, and by subsequent sputtering deposition of the magnetic material [89]. Typical pinning structures consist in arrays of 50×50 coin-shaped Fe dots with diameters ranging between 250 and 350 nm and heights between 10 and 15 nm. As an example, figure 5 shows scanning electron microscopy images of square and hexagonal patterns of dots and a typical height profile of the structure obtained with atomic force microscopy. The application of this type of pinning to induce symmetry transitions in $Bi_2Sr_2CaCu_2O_8$ and $NbSe_2$ vortex matter is presented in sections 5 and 6, respectively. In this review the discussion is limited to the case of the first matching field. The effect of decommensuration between vortex and pinning structures was studied in [90].

Recently, two reports have presented new approaches to study symmetry transitions in three-dimensional vortex matter. In the first one, scanning tunnelling microscopy was used to image the vortex structural transition induced by a square array of gold dots introduced in $NbSe_2$ crystals [92], see figure 3(i). In the second study, scanning Hall probe microscopy was applied to visualize individual vortices in a Sr_2RuO_4 crystal with a square array of focused ion beam milled holes [93]. More studies are desirable in order to gain further insight into the problem discussed here.

4. Magnetic-decoration imaging of structural transitions in vortex matter

The methods to image the VS in real space with single-vortex resolution are sensitive either to the superconducting order parameter local depletion (on lengthscales of the order of ξ) or to the variation of the local magnetic induction (on lengthscales of the order of λ). Scanning tunnelling microscopy [102–105] is the unique technique sensitive to the spatial variation of the superconducting order parameter inherent to a vortex. The methods sensitive to λ are magnetic decoration [4, 74, 75, 78, 106–111], Lorentz microscopy [96, 112], magnetic force microscopy [113–116], scanning SQUID microscopy [117–124], scanning Hall probe microscopy [72, 86, 120, 125–128], scanning electron microscopy [129] and magneto-optical imaging [130].

The magnetic-induction and scan ranges in which every technique was applied to resolve individual vortices are summarized in figure 6. Scanning tunnelling microscopy surveys areas of typically μm^2 and is therefore employed to image vortices in the tesla range [102–105]. The techniques that rely on the magnetic-induction spatial variation lose single-vortex resolution for vortex spacings of the order of the penetration depth. Those that are based on the detection of stray fields at nanosized or micron-sized distances from
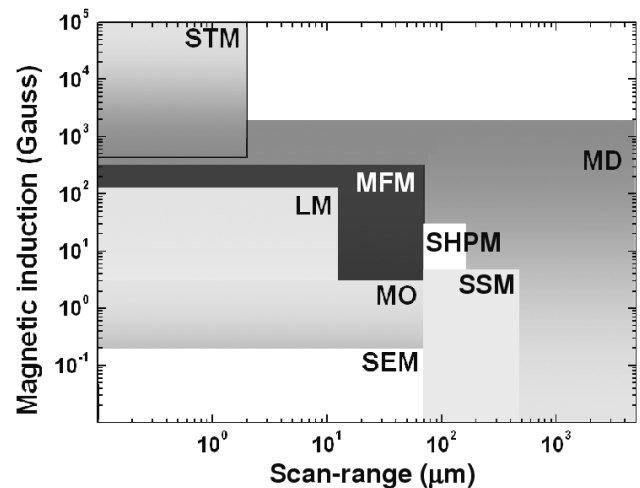
Figure 6. Single-vortex resolution with different experimental techniques: range of magnetic induction versus scan-range. The abbreviations used are: scanning tunnelling microscopy (STM), magnetic decoration (MD), Lorentz microscopy (LM), magnetic force microscopy (MFM), scanning SQUID microscopy (SSM), scanning Hall probe microscopy (SHPM), scanning electron microscopy (SEM) and magneto-optical imaging (MO). The abbreviations are placed on the top-right corner of the rectangle that depicts the range of application of the techniques.

the sample surface achieve single-vortex resolution only up to moderate fields: a few tens of gauss in the case of scanning Hall probe microscopy [62, 72, 86, 127] and magnetic force microscopy [113, 115, 116, 131] and a few gauss for magneto-optical imaging [130]. Lorentz force microscopy allows the imaging of single vortices up to densities of $\sim$100 G [96] and in fields of view of the order of 100 μm^2. Scanning SQUID microscopy, with the higher flux sensitivity of $10^{-6}\Phi_0/\sqrt{(Hz)}$ [132], resolves individual vortices up to several gauss [91, 120–122, 124, 133].

The application of magnetic-imaging techniques to resolve individual vortices in high-T_c materials remains quite limited since the greater value of λ in these materials significantly reduces the spatial resolution. By using scanning SQUID [120, 121], scanning Hall probe [119, 120] and magnetic force [116] microscopies vortices in high-T_c materials were imaged up to fields of only some gauss.

In contrast, the magnetic-decoration technique resolves individual vortices for a range of applied fields significantly broader, up to the record of 1840 G [111]. This is a consequence of the direct contact between sample and probe: the magnetic particles that decorate vortex positions are allowed to land on the very surface of the sample. In order to study structural symmetry transitions in static conditions the magnetic decoration is a suitable technique because it has the merit of imaging with single-vortex resolution thousands of vortices (field of view of the size of the sample). Besides, this imaging method can be implemented in low- as well as high-T_c materials. In the latter case it was successfully applied to image the vortex structure at different temperatures [134].

As discussed in the previous section, the application of these techniques to directly image structural transitions in three-dimensional vortex matter remains still quite reduced. In
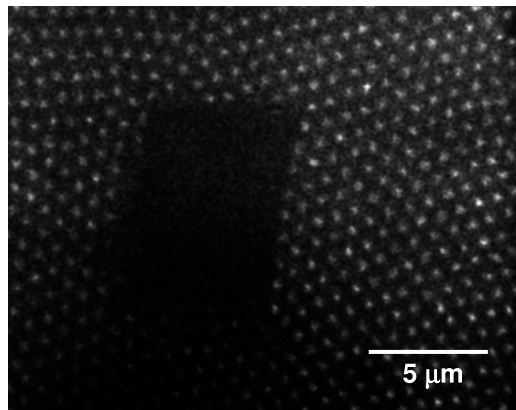
Figure 7. Scanning electron microscopy image of the Fe agglomerates resulting from a magnetic decoration of the NbSe$_2$ vortex structure. In the 6×8 μm^2 central region the decoration agglomerates were washed off by scanning the surface with the tip of an atomic force microscope (working in the force mode with a force of 1 nN).

Figure 8. Atomic force microscopy image of the decoration agglomerates with a protective 100 Å gold layer in a Bi$_2$Sr$_2$CaCu$_2$O$_8$ sample. The VS was generated at a field of 36 Oe. Three- (a) and two-dimensional (b) image of a 5×5 μm^2 field of view. (c) Height profile along the black line overlayed in (b). Reprinted with permission from [81]. Copyright (2000) by the American Physical Society.

particular, the study of the dynamics of structural transitions is limited by the acquisition time that has to be smaller than the characteristic timescales of vortex motion. Lorentz microscopy, with frame-imaging times that can be as short as 30 ms, was applied to image vortex motion when ramping the field, but only in the case of thin films [76]. The use of magnetic decoration to image single-vortex dynamics is limited because every experiment is a snapshot taken during a typical decoration-time of seconds. Despite this drawback, it has been successfully applied to image the penetration pattern of vortices when increasing the magnetic field [109, 135, 136] and the vortex-critical-state dynamics at low fields [110, 137]. Therefore magnetic decoration can also be used, though in limited experimental conditions, to image the dynamics of structural transitions in vortex crystals.

4.1. Magnetic-decoration working principle

The magnetic-decoration technique is also known as 'Bitter magnetic decoration' because Bitter implemented it back in 1931 to study magnetic domain walls in ferromagnets [138]. In his pioneering work he used a colloidal suspension of magnetic particles in alcohol in order to *decorate* the regions of the sample presenting local magnetic field inhomogeneities. A similar experimental approach using Ni particles in liquid helium was applied to image magnetic-flux patterns in type-I superconductors [139]. Later, magnetic particles were generated by the evaporation of a metal in an inert gas and used to decorate ferromagnetic domain boundaries [140].

Ten years after Abrikosov's theoretical suggestion [17] of the existence of vortices in type-II superconductors, the magnetic-decoration technique was used by Essmann and Träuble to image the VS in real space for the first time [4]. These studies were crucial in order to provide irrefutable evidence for the existence of vortices and confirm that the magnitude of the vortex flux quanta is $\Phi_0 = hc/2e$. Ferromagnetic particles were evaporated in a helium atmosphere in order to decorate individual vortices in In-doped

Pb and pure Nb [4]. This implementation of the technique is the one generally used nowadays.

The magnetic-decoration working principle is based on the spatial modulation of the local magnetic induction inherent to vortices: $h(\vec{r})$ is maximum at the vortex centre and, for bulk superconductors, decays exponentially over a length λ [5]. The magnetic flux of a vortex spreads out from the sample over a length in the longitudinal direction of the order of λ [5]. The stray-field gradient exerts a magnetic force on the evaporated magnetic nanoparticles. As a result, they are attracted towards the vortex core and 'decorate' a region of size λ. The nanoparticle agglomerates remain attached to the sample surface due to van der Waals forces. This allows the observation of the VS replica pattern at room temperatures using scanning electron [78] or transmission electron [141] microscopies.

The topographic properties of the Fe pattern resulting from a magnetic decoration can be characterized by means of atomic force microscopy. This is not a straightforward experiment since the adhesion force of the agglomerates to the sample surface is weak. This is illustrated in figure 7: the Fe agglomerates can be washed off with the tip of an atomic force microscope even with a force of 1 nN (image taken in force mode). However, sputtering a 100 Å thick gold layer on the decorated surface allowed us to perform topographic measurements by means of atomic force microscopy. Figure 8 shows a typical image obtained in a decorated Bi$_2$Sr$_2$CaCu$_2$O$_8$ crystal with a force of 1 nN. Agglomerates are cone-shaped, and for a magnetic decoration at 36 Oe statistics reveal average
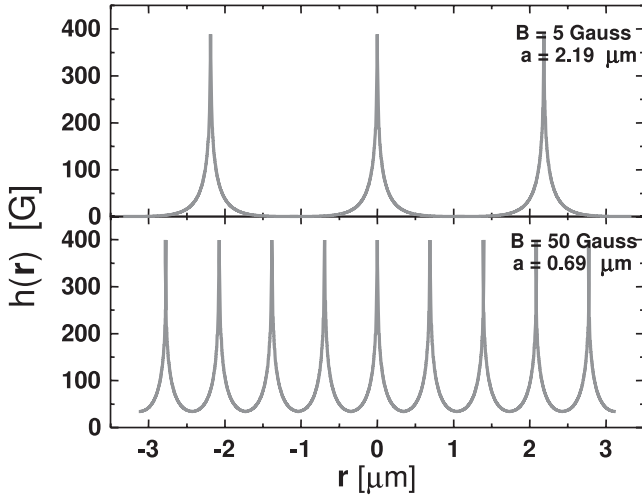
Figure 9. Profile of local magnetic induction, $h(r)$, on the bulk of a $Bi_2Sr_2CaCu_2O_8$ sample at 4.2 K (λ(4.2 K) = 2000 Å). Macroscopic magnetic inductions, B, are (a) 5 and (b) 50 G.

height and diameter of 600 Å and 2000 Å, respectively. In the central part of the sample the dispersion of height values is roughly 3%. In regions located within 10 μm of the sample edge the height of the agglomerates decreases significantly.

Magnetic decorations are typically performed by Joule evaporation of a magnetic material (Fe, Ni, Co) wound on a tungsten filament. This is done in an inert gas atmosphere, typically helium, at pressures of the order of 100 mTorr. Since the mean free path at this pressure range is of the order of micrometres, during its diffusive spreading out the atoms scatter with the inert gas molecules, thermalizing at the gas temperature [142] and forming clusters of roughly 50 Å in diameter [143–145]. The clusters diffuse in the decoration chamber and at distances from the sample $\sim\lambda$ are attracted towards the vortex positions. The deposition of clusters on the surface of the sample occurs during seconds [146].

When vortices penetrate a sample a spatial variation of local magnetic induction, $\vec{h}(r, z)$, is established ($\vec{h}(r, z) = \vec{h}(r)$ well in the interior of the sample). This gradient exerts an attractive force on the evaporated clusters of magnetic moment $\vec{M}$ given by

$$\vec{F}_m = |(\vec{M} \cdot \vec{\nabla})\vec{h}(r)|. \quad (5)$$

The modulus of the local magnetic induction has its maximum, h_{max}, at the vortex core. In the limit of low vortex densities it can be approximated by $h_{max}(0 < r < \xi) \approx 2H_{c1}$, where H_{c1} is the field at which the first vortex penetrates the sample. The minimum value of the local magnetic induction, h_{min}, is found at the midpoint between vortices, $a(B)/2$. The magnitude of h_{min} depends on the relation between the lattice parameter and the penetration depth $\lambda(T)$ [147–149]. In the magnetic field range where $a(B) \geqslant 4\lambda$ the local induction reaches it minimum value $h_{min} \approx 0$; see figure 9(a). For fields such that $a(B) < 4\lambda$ the supercurrents of adjacent vortices overlap, producing $h_{min} \approx 4H_{c1}\exp(-a/2\lambda)$, and the gradient of the local magnetic induction decreases; see figure 9(b).

The spatial resolution of the Bitter decoration on increasing the magnetic field is limited by the overlap of

the $h(r)$ of adjacent vortices. In order to decorate vortices the magnetic energy of the clusters must be greater than its kinetic energy, $E_{mag} \approx M\Delta H > k_B T$ [150], where $\Delta H = h_{max} - h_{min} = 2H_{c1}(1 - 2\exp(-a/2\lambda))$. Considering that the magnetic moment of a cluster is $M = \mu V$ with μ the magnetization per unit volume, in order to decorate vortex positions the cluster volume must exceed the threshold value

$$V_{th} = k_B T/\Delta H\mu = k_B T/(2H_{c1}\mu(1 - 2\exp(-a/2\lambda))). \quad (6)$$

Since ΔH decreases with magnetic field, V_{th} increases. At a given value of the magnetic field the threshold dimension will reach the vortex lattice spacing, $V_{th} \sim a^3(B)$, and individual vortices will no longer be resolved.

The maximum magnetic field at which individual vortices are resolved inversely depends on the penetration depth, given that the threshold volume decreases when reducing λ. For example, magnetic decorations in the high-T_c material $Bi_2Sr_2CaCu_2O_8$ with $\lambda \sim 2000$ Å achieve single-vortex resolution up to fields of the order of 100 G [151], whereas in the borocarbide material $LuNi_2B_2C$ with $\lambda \sim 760$ Å [152], individual vortices are decorated at the record magnetic field of 1840 G [111].

In a magnetic-decoration experiment the volume of the clusters is determined by the inert-gas density, increasing when raising the pressure. This is the key parameter to control in order to succeed in imaging individual vortices by magnetic decoration. In our experimental set-up [151], typical decoration pressures range between 50 and 250 mTorr at temperatures around 4.2 K. The optimal pressure (size of clusters) has to be adjusted depending on the λ of the material and on the particular temperature and magnetic field at which the experiment is performed.

In order to improve the field sensitivity of the magnetic-decoration technique, maximizing the value of μ is crucial. Therefore the formation of domain walls and surface oxidation is avoided and materials with a high magnetization per atom are evaporated. Pure iron is a good choice because it has one of the highest μ values among the ferromagnetic pure elements (2.2 against 1.72 and 0.61 μ_B/at for Co and Ni, respectively) [142]. In the pressure range at which magnetic decorations are performed, the typical dimensions of Fe clusters are such that they are single magnetic domains [56, 144]. The oxidation of the clusters is minimized by evaporating the particles in an inert-gas atmosphere.

A critical condition to decorate vortices is that the sample temperature remains as stable as possible during the decoration process. The evaporation of the magnetic particles is performed at temperatures of the order of 2000 K. The sample, placed typically at some centimetres from the filament [151], must not warm considerably during the decoration process. Good thermal contact between the sample holder and the cryogenic bath is generally not enough to avoid sample heating and therefore a baffle is placed between the sample and the filament in order to decrease the heat radiation [151]. In spite of these precautions, for example, in the insert used to perform the experiments described in following sections the sample heats around 0.5 K during the decoration process [153].

4.2. Magnetic-decoration imaging of induced vortex structural transitions: state of the art and challenges

The reports on imaging vortex structural transitions with the magnetic-decoration technique refer to experiments performed in field-cooling (FC) conditions, i.e. the sample is cooled down to low temperatures with a field applied at $T > T_c$. On cooling below a temperature $T_i < T_c$ pinning sets in and the magnetic response of the vortex system becomes irreversible. At this temperature the pinning energy overcomes the vortex–vortex interaction energy and the local pinning barriers inhibit vortex displacements on distances larger than $\xi \ll a$ (for low fields) [26]. Therefore the VS freezes at the lattice parameter lengthscale and the structure decorated at low temperatures presents the topological properties of that frozen at T_i [154, 155].

For low-T_c materials, when cooling through the second-order phase transition at $T_{c2}(H)$ vortices nucleate, and pinning sets in at almost the same temperature. For example, in the case of NbSe$_2$ local magnetic induction combined with magnetic decoration [8, 155], bulk magnetization and susceptibility [156] experiments found $T_i \sim T_{c2}$ for $B < 100$ G. In contrast, in high-T_c superconductors vortices continuously nucleate at the crossover temperature T_{c2} and a liquid vortex phase is stable at $T \lesssim T_{c2}$. On further cooling, at low fields the vortex liquid undergoes a first-order solidification transition at $T_m(H)$, and pinning sets in at a temperature $T_i < T_m$. In the particular case of the platelet-like samples of Bi$_2$Sr$_2$CaCu$_2$O$_8$ studied in section 5, magnetization and susceptibility measurements show that within the experimental error T_i coincides with T_m for $B < 100$ G [32, 41].

As mentioned in the previous section, the second report on the application of the magnetic-decoration technique to image the effect of periodic pinning structures studied the nucleation of vortices in blindholes patterned in Nb films [77]. In these experiments the film thickness and the bottom thickness of the blindholes were always larger than or of the order of the penetration depth of the bulk material, $\lambda = 400$ Å. In this case the vortex supercurrents decay exponentially with distance, $j_{\text{vortex}} \sim \exp(-r/\lambda)$, as in a bulk superconductor [5]. Therefore, the magnetic field around the vortex decays on a length λ and the spatial resolution of the magnetic decoration will be given by this magnitude, as in the case of crystals.

Performing this type of experiment in thin films is technically more difficult. In the case of a very thin film with $t \ll \lambda$ it has been calculated [157–159] and verified experimentally [160, 161] that the decay of the vortex supercurrents is weaker than in a bulk sample: $j_{\text{vortex}} \sim 1/r$ from the vortex centre up to $r = 2\lambda^2/t$ and $j_{\text{vortex}} \sim 1/r^2$ for greater distances. In this case the magnetic size of vortices is considered as $2\lambda^2/t \gg \lambda$. As a consequence, the local induction modulation is smaller for a thin film ($t < \lambda$) than for a crystal of the same material, which seriously limits the individual-vortex resolution of the magnetic-decoration technique. In fact, only three works report on magnetic decoration of vortices in pristine thin films [108, 162, 163]. The magnetic-decoration imaging of structural transitions in thin films still remains quite a challenging experiment.
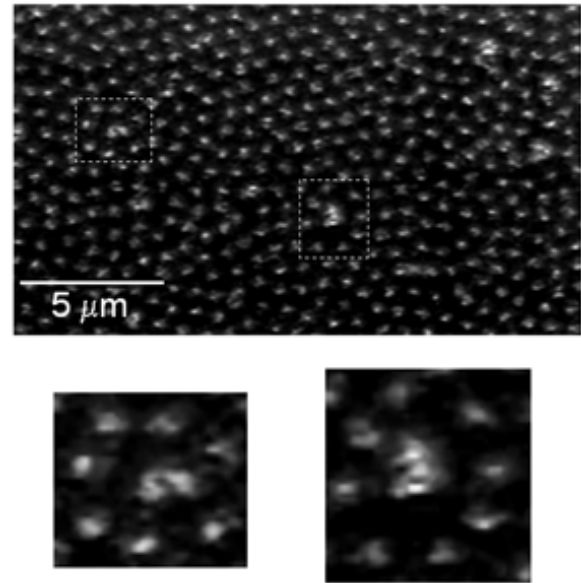
Figure 10. Magnetic-decoration image of Bi$_2$Sr$_2$CaCu$_2$O$_8$ vortex matter nucleated in a sample with randomly distributed columnar defects. The density of vortices is $B = 4B_\Phi$, with $B_\Phi = n_p\Phi_0 = 10$ G the density of columnar defects. Insets: enlarged images of areas framed in the main panel. (Data from [164].)

This difficulty is not present in the case of three-dimensional vortex matter. The magnetic decoration has been successfully applied to image pinning-induced vortex structural transitions in three types of experiment. One is the imaging of vortices nucleated in crystals with periodic pinning structures generated by electron beam lithographed Fe dots [25, 89, 90, 99–101]. Paradigmatic examples of these experiments will be presented in the two following sections. As discussed in section 3, the other two classes of experiment were performed using a pinning structure that is a replica of the VS, the Bitter pinning [78, 79, 81], and a random distribution of columnar defects [74, 75, 88]. In the three cases the magnetic-decoration spatial resolution is only limited by the value of λ of the materials.

As the magnetic decoration replicates the location of the maxima in $h(r)$, the number of flux quanta per Fe agglomerate cannot be directly measured. In pristine crystals with a point-like distribution of weak pinning centres, multiple quanta of flux per agglomerate are not likely since the gain in pinning energy is not enough to overcome the repulsive interaction between vortices. In contrast, in samples with strong pinning sites, such as columnar defects, twin boundaries or stacking faults, some agglomerates can encompass multiple quanta of flux. For example, figure 10 shows the agglomerates resulting from a magnetic decoration of the VS nucleated in a sample with a relative density of columnar defects $n_p = B_\Phi/\Phi_0 = 0.25n_v$ [164], where B_Φ is the matching field. Since the distribution of columnar defects is at random, there is a finite probability that two or more defects lie close to each other, in particular closer than λ. In this case, if each of these defects is occupied by a vortex, a decoration experiment will not be able to resolve individual vortices because a single Fe agglomerate will be observed. In the framed areas of

figure 10 some agglomerates have an irregular and bimodal shape, suggesting they encompass two flux quanta. In the case of the experiments presented in the following sections, where vortices are nucleated in regions patterned with magnetic dots, Fe agglomerates decorate only one vortex. This was concluded after finding that the density of agglomerates, regular in shape, is the same in pristine than in non-patterned areas.

5. Vortex structural transitions involving plastic deformations: the case of Bi$_2$Sr$_2$CaCu$_2$O$_{8-\delta}$

The experiments presented in this section were performed in Bi$_2$Sr$_2$CaCu$_2$O$_8$ crystals patterned at the surface with Fe-dot pinning structures generated by means of electron beam lithography as described in section 3.2 (see figure 5 for a scanning electron microscopy image of the pinning structure). The VS was nucleated in the range of magnetic induction $0 < B \lesssim 30$ G. In order to discuss the effect of this surface pinning, we first survey the topological properties of the Bi$_2$Sr$_2$CaCu$_2$O$_8$ VS nucleated in pristine samples.

At this point, it is worth mentioning that the steps generated at the surface of Bi$_2$Sr$_2$CaCu$_2$O$_8$ samples when cleaving also constitute an additional pinning potential [165]. This is because, in the vicinity of a step, when vortices are located in the thinner part of the sample its line energy is reduced by a factor $s\epsilon_L$, where s is the step height and $\epsilon_L = (\Phi_0/4\pi\lambda)^2 \ln\kappa$ the vortex-line energy per unit length. If the steps are high and long enough, grain boundaries that separate domains with different orientations are formed along the whole sample thickness [6, 165]. Therefore, in the experiments discussed in this section and the next the topology of the VS was studied in regions where the sample was flat as observed by scanning electron microscopy.

Figure 11 shows a typical magnetic-decoration image taken after nucleating the VS in an FC process. The magnetic decoration was performed at 4.2 K, but as discussed in section 4.2 the observed structure corresponds to that frozen at $T_i \sim T_m$ [32, 41] for the platelet-like samples studied in this section. The low-field Bi$_2$Sr$_2$CaCu$_2$O$_8$ VS has long-range orientational order, as expected for the Bragg glass phase [22, 23, 25]. The structure also presents a low (2%) density of edge dislocations that suppresses the positional order at the local scale. This is at odds with the theoretical result that the Bragg glass lacks topological defects at equilibrium [20, 21, 27, 28]. However, magnetic-decoration studies as a function of temperature [134] and up to magnetic fields of 120 G [23] indicate that the observed dislocations are out-of-equilibrium features that have their origin in the quenched dynamics of FC processes.

The positional order of the structure can be characterized by the positional correlation function, $G_K(\vec{r})$, obtained considering the translational order parameter [166]

$$\Psi_{K_l}(\vec{r}_i) = \exp(i\vec{K}_l \cdot \vec{r}_i) \qquad (7)$$

that quantifies the displacement of the ith vortex with coordinate $\vec{r}_i$ from the sites of a perfect hexagonal lattice with reciprocal vectors $\vec{K}_l$. The perfect hexagonal lattice is constructed considering its $\vec{K}_l$ vectors to be equal to those
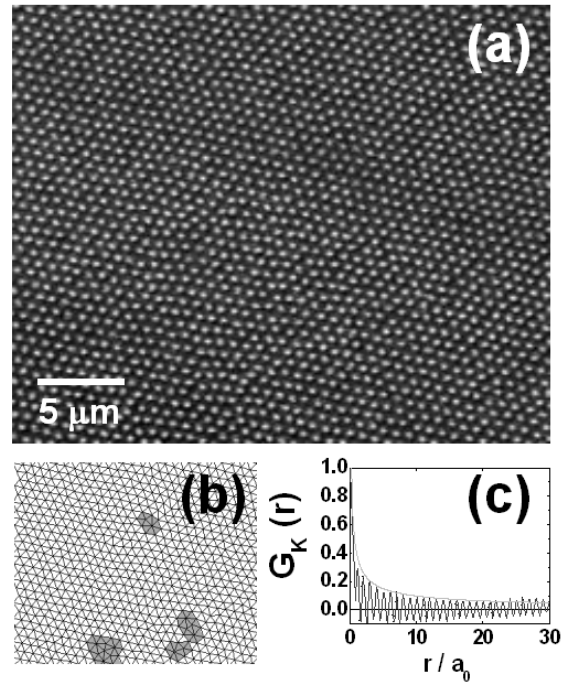
Figure 11. Structural properties of the field-cooled Bi$_2$Sr$_2$CaCu$_2$O$_8$ vortex structure at low fields ($B = 36$ G). (a) Magnetic-decoration image of the VS. (b) Delaunay triangulation of the lower-right region of the image. First neighbours are bonded with lines and non-sixfold coordinated vortices are depicted in grey. (c) Positional correlation function evaluated in a dislocation-free region containing of the order of 10^3 vortices. The grey line is a fit of the envelope with a power-law decay. Reproduced from [25], copyright 2005 by The National Academy of Sciences of the United States of America, all rights reserved.

where the Fourier transform of the experimental structure presents a maximum. The correlation function,

$$G_{K_l}(r) = \langle \Psi_{K_l}(0)\Psi_{K_l}^*(r) \rangle = \frac{1}{N(r)} \sum_{i,j} \Psi_{K_l}(\vec{r}_i)\Psi_{K_l}^*(\vec{r}_j), \qquad (8)$$

measures the average vortex displacements as a function of distance. The averaging is performed over the $N(r)$ pairs of single vortices separated by a distance $r = |\vec{r}_i - \vec{r}_j|$. Since bulk pinning consists in a random distribution of pinning sites, the positional correlation function considered in this work, $G_K(r)$, is an average of the three $G_{K_l}(r)$. Figure 11(c) shows that $G_K(r)$ decays as a power law at long distances [23, 25], as expected for the Bragg glass phase. This calculation was done in a dislocation-free region containing roughly 1000 vortices.

Different experimental realizations for the same magnetic field have similar $G_K(r)$, but the particular positions of vortices change in every realization. As shown in figure 4, the Bitter pinning that replicates the VS is able to break this degeneracy. It is then interesting to explore whether an equally weak but periodic pinning can render the Bragg glass unstable.

5.1. Structural transitions induced at the surface of the vortex crystal

The first attempt to explore the stability of the Bragg glass consisted in nucleating the Bi$_2$Sr$_2$CaCu$_2$O$_8$ VS in first
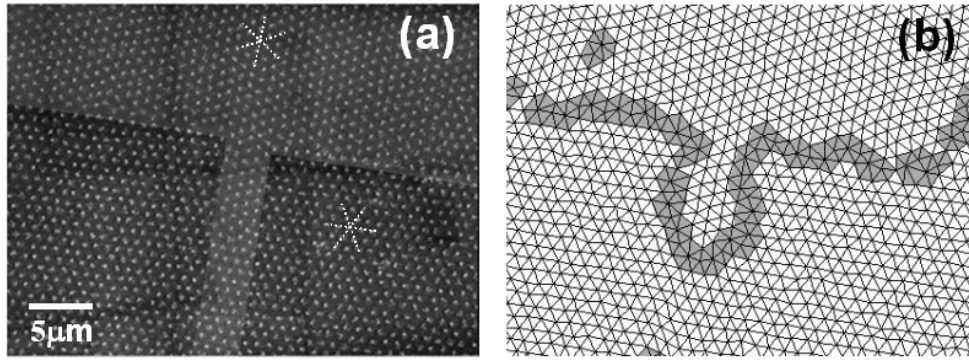
Figure 12. $Bi_2Sr_2CaCu_2O_8$ vortex matter interacting with a hexagonal surface pinning at the first matching condition ($B = 30.9$ G). (a) Magnetic-decoration image of the FC structure nucleated in pristine and patterned regions (darker background). Dotted lines depict the compact planes of the structure in both regions (b) Delaunay triangulation of the VS where non-sixfold coordinated vortices are depicted in grey. Reproduced from [25], copyright 2005 by The National Academy of Sciences of the United States of America, all rights reserved.
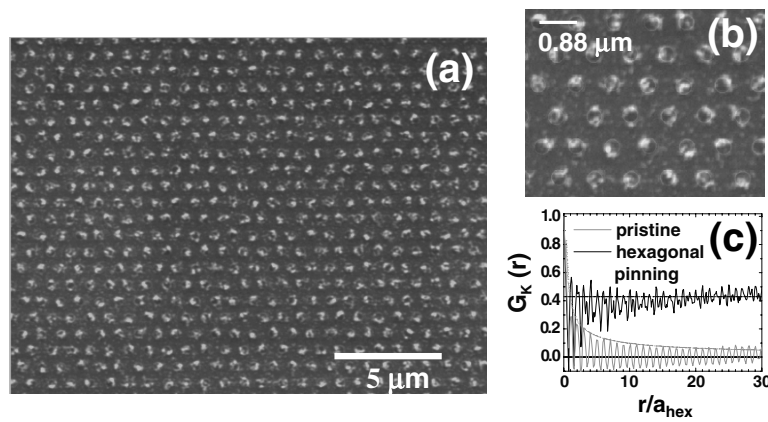
Figure 13. (a) High-amplification image of the long-range ordered $Bi_2Sr_2CaCu_2O_8$ vortex structure induced by the hexagonal surface pinning. (b) High-resolution image where the irregular shape of the decoration agglomerates contrasts with the perfectly circular shape of the pinning sites. (c) Positional correlation functions of the VS nucleated in pristine and patterned regions. For the latter case, the fluctuation around a value of 0.43 for long distances reveals that the structure has long-range positional order.

matching condition with a perfectly hexagonal surface-pinning potential. Figure 12(a) shows a magnetic-decoration image of the VS nucleated in patterned and pristine regions of the sample. In the patterned regions the principal directions of the VS are parallel to those of the pinning structure. In the pristine regions this is generally not the case, resulting in the formation of topological defects at the pinning-pattern edge. This indicates that the surface pinning is effective at a temperature higher than the one at which bulk pinning sets in, $T_i \sim T_m$.

In the patterned regions, including 2500 vortices per pattern, the VS presents no dislocations. Moreover, the higher amplification image of figure 13(a) reveals that vortices match the pinning structure and are located within the dot radius. This indicates that the surface pinning is effective at transforming the quasi-long-range positionally ordered VS into a long-range ordered hexagonal lattice, at least at the surface of the vortex crystal.

The bulk pinning also affects the VS in a smaller lengthscale: it induces angularly random and non-cumulative vortex displacements with respect to the centre of the pinning sites. The amplitude of these displacements is smaller than or of the order of the dot radius, R_D. This is reflected as a

positional correlation function that fluctuates around a finite value $G_K < 1$, for distances $r \gtrsim 5a_{hex}$ (a perfect lattice has $G_K = 1$ at all distances). Assuming that the random vortex displacements follow a Gaussian distribution with average δ, the positional correlation function can be expressed as

$$G_K(r) = \langle \exp(i\vec{K} \cdot \vec{\delta})^2/2 \rangle \approx 1 - 1/2\langle(\vec{K} \cdot \vec{\delta})^2\rangle. \quad (9)$$

Since at long distances $G_K \approx 0.43$, the average amplitude of vortex displacements around the centre of the hexagonal pinning sites can be estimated as $\delta_{hex} \sim 0.17a_p \sim R_D$ ($a_p = 0.88$ μm and $R_D = 130$ nm).

The observed random vortex displacements can be explained by considering a Debye–Waller factor resulting from an effective temperature associated with the effect of bulk pinning. The ratio between the standard deviation of the first-neighbours' distance distribution (SD $= (1/N)\sum_i (a_i - \langle a \rangle)^2$) and the average vortex spacing ($\langle a \rangle$), $\sigma = \sqrt{SD}/\langle a \rangle$, is a measure of this Debye–Waller factor. In fact, σ is 18% smaller in patterned than in pristine regions; see figures 14(a) and (b). The effective Debye–Waller temperature should decrease by reducing R_D. This is confirmed by
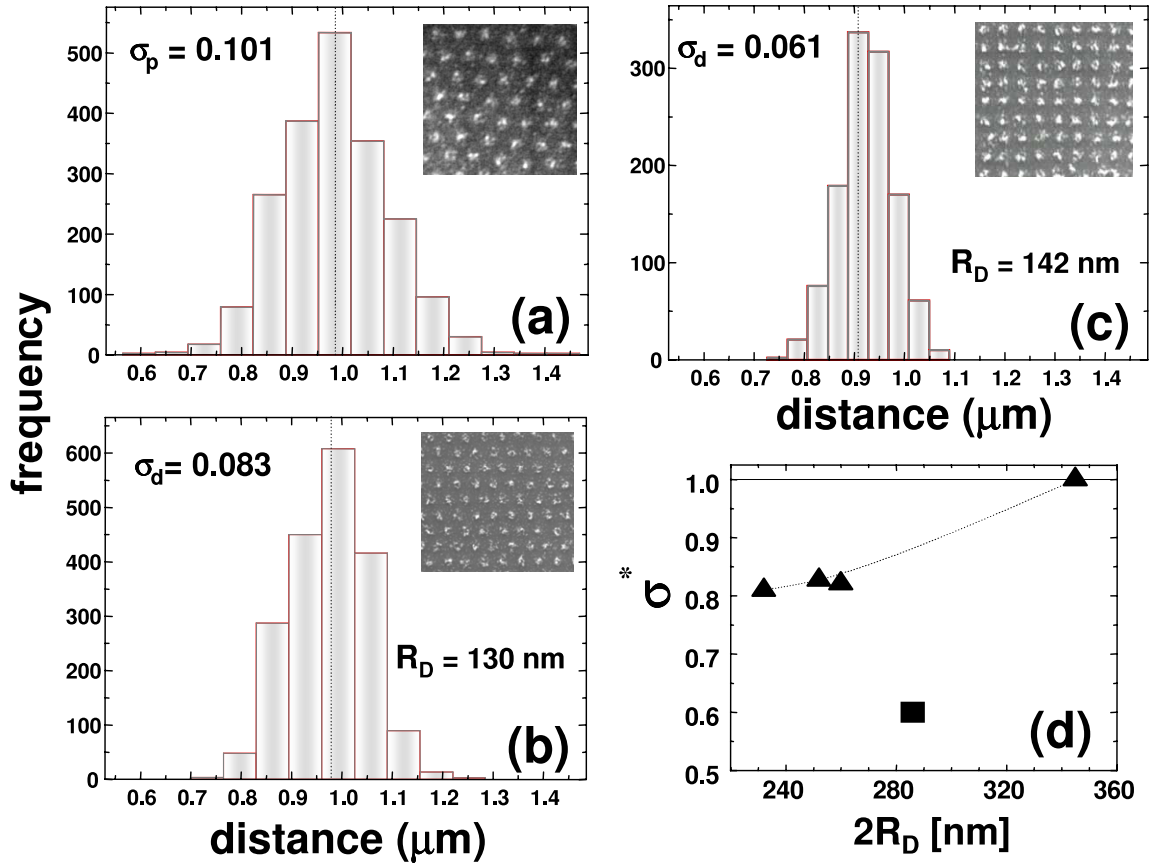
Figure 14. Distributions of first-neighbours' distance for experiments in the first matching field. (a) Pristine areas [25] and regions with (b) hexagonal [25] and (c) square arrays of dots. (d) Normalized standard deviation $\sigma^\star = \sigma_d/\sigma_p$, with σ_d evaluated in patterned and σ_p in pristine regions, as a function of dot radius, R_D. The triangular and square symbols refer to the hexagonal and square arrays of pinning centres, respectively. In all cases $B = 25$ G and the lattice parameters of pinning structures are $a_{hex} = 0.98$ μm and $a_{sq} = 0.91$ μm. The images used to extract these data have a high spatial resolution of 0.02 μm per pixel.

the results shown in figure 14(d): the normalized standard deviation $\sigma^\star = \sigma_d/\sigma_p$, ($\sigma_d$ and σ_p are the standard deviations of the structures nucleated in patterned and pristine regions, respectively) decreases on reducing R_D. This result also indicates that the localization of vortices within R_D is due to a collective response of the vortex structure nucleated in the presence of the periodic pinning [25].

A stringent condition to test whether a weak surface pinning can render the Bragg glass unstable is to try to induce a symmetry transition of the VS. With this aim, square arrays of pinning centres such as the one shown in figure 5 were engineered at the surface of the samples. The VS was nucleated in the first matching condition; therefore, the lattice parameters of the vortex (a_{hex}) and pinning (a_{sq}) structures $a_{hex} = 1.075a_{sq}$.

The magnetic-decoration image of figure 15 reveals that this pinning structure induces a square VS at the surface. This hexagonal-to-square symmetry transition is accomplished in lateral distances of only one unit cell, at the edge of the patterned areas. The inherent reduction of the lattice parameter increases the vortex–vortex interaction energy of the square crystal of 2500 vortices by a factor of 2%. The surface pinning acting at roughly one hundredth of the vortex length accounts for this symmetry transition.

The induced square VS has long-range positional order, as revealed by the fluctuation of $G_K(r)$ around a finite value ≈ 0.77 for distances $r > 5a_{hex}$; see figure 15. As in the case of the hexagonal pinning, the long-range order stems from the confinement of vortices within pinning sites. The effect of bulk pinning is also manifested as random vortex displacements with respect to the centre of dots. Assuming once more that these displacements follow a Gaussian distribution, equation (9) gives an average amplitude $\delta_{sq} \sim 100$ nm $\sim 0.7R_D$ ($R_D = 142$ nm).

Strikingly, the square array of dots seems to pin vortices more efficiently than the hexagonal one. This can be concluded from the greater asymptotic value of $G_K(r > 5a_{hex})$ for the square (0.77) than for the hexagonal (0.43) VS, in accordance with $\delta_{sq} = 0.77\delta_{hex}$. More evidence is provided by the 25% smaller value of σ for the square than for the hexagonal vortex structure; see figures 14(b)–(d). This effect does not have a trivial origin by the fact that vortices in the square structure are more restrained than in the hexagonal one since σ is calculated by normalizing the standard deviation of first-neighbours distance with the average vortex spacing.

These results seem counterintuitive if a naïve energetic argument is considered: for the square pattern part of the pinning-energy gain accounts for the increase of vortex–vortex
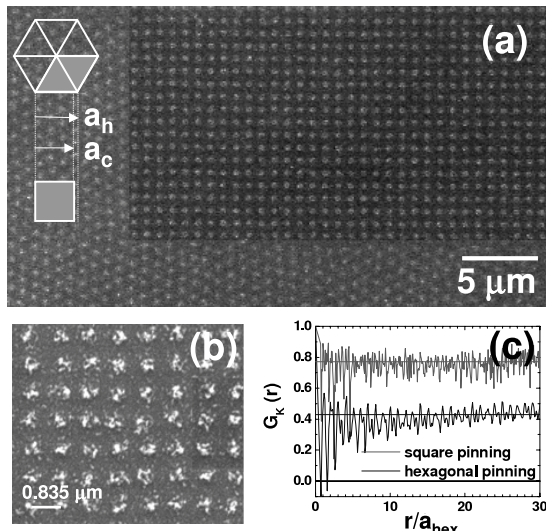
Figure 15. $Bi_2Sr_2CaCu_2O_8$ vortex matter interacting with a square array of surface-pinning centres in the first matching condition ($B = 29.7$ G, $a_{sq} = 0.835$ μm) (a) magnetic-decoration image of the FC vortex structure nucleated in pristine and patterned regions (darker background). (b) High-resolution image of the induced square VS. (c) Positional correlation functions of the vortex structure nucleated in regions with square and hexagonal pinning potentials.

interaction energy, whereas for the hexagonal pinning the last term is zero and vortices would be better pinned at the surface. As this is not observed, an extra energy term has to be considered in order to explain these results. In the case of the two-dimensional VS nucleated in films with periodic pinning arrays this phenomenon is also observed: vortex dissipation versus B curves present more and deeper minima for pinning structures with square symmetry [167]. As a consequence, the extra energy term cannot be exclusively associated with the three-dimensional nature of vortices in $Bi_2Sr_2CaCu_2O_8$. Further experimental as well as theoretical [168–170] studies are needed in order to understand the origin of this finding.

5.2. Structural transition induced along the direction of vortices

Since three-dimensional vortex matter is elastic in nature, the square VS induced at the surface will no longer be stable in the bulk of the sample. The natural hexagonal symmetry of the VS will be recovered at a distance of a few lattice parameters beneath the surface. This situation allows the use of vortex matter as a laboratory system to visualize with microscopic resolution transformations between structures with different symmetries.

Microscopic access to this square-to-hexagonal transition was gained by engineering the pinning structure at the sample's top surface and performing magnetic decorations at the bottom surface for different thicknesses [89]. The experimental realization consisted in gluing the top surface of the sample on a decoration sample holder and in successively cleaving the bottom surface. The easy-cleavable nature of $Bi_2Sr_2CaCu_2O_8$ allowed us to perform experiments in the same sample for thicknesses t ranging from half to hundreds of vortex unit cells.
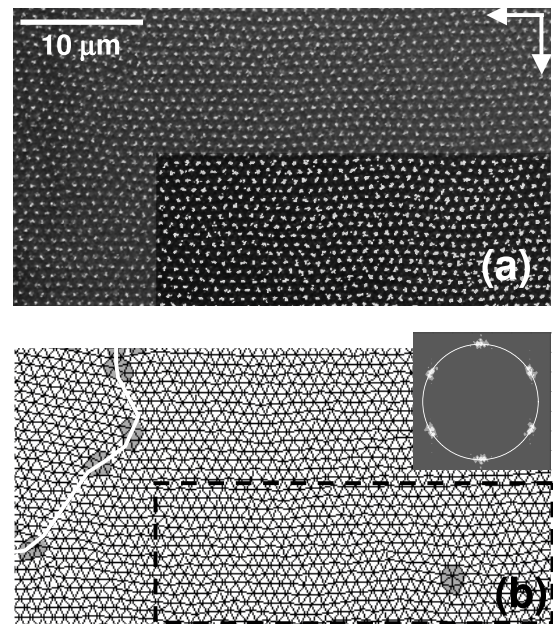
Figure 16. Magnetic decoration of the $Bi_2Sr_2CaCu_2O_8$ vortex structure at the bottom surface for a thickness of (4.5 ± 0.3) μm. (a) Vortex structure in pristine and beneath patterned (darker background) areas. Arrows indicate the [10] and [01] directions of the top-surface square pattern. (b) Delaunay triangulation, where the frame indicate the edge of the patterned region. Inset: Fourier transform of the bottom-surface VS located beneath the pinning structure.

In all cases the magnetic field ($B = 26.1$ G) was set in order to have the same density of vortices as that of pinning sites ($a_{sq} = 0.89$ μm).

Hexagonal vortex structures are observed for thicknesses t between (100.0 ± 0.3) and (4.5 ± 0.3) μm. A Fourier transform analysis reveals that the VS nucleated beneath the pinning structure is isotropic; see figure 16. This means that the deformation induced at the top surface is completely relaxed for $t \geqslant 4.5$ μm. In patterned regions the bottom-surface VS typically presents one compact plane parallel to a principal direction of the square pinning. In pristine regions the VS orientation is not determined by the pinning pattern and varies from one experimental realization to another. Therefore the top-surface pinning breaks the rotational symmetry of the VS nucleated in the patterned region.

On further cleaving, for (0.5 ± 0.3) μm $< t < (4.5 \pm 0.3)$ μm an interface between the top-surface square and the bottom-surface hexagonal vortex structures is detected. For the smallest thickness achieved, (0.5 ± 0.3) μm, a square VS is observed at the bottom surface; see figure 17. This implies that the top-surface square VS propagates as a three-dimensional structure down to a thickness of the order of the VS lattice parameter, $t_{pr} \sim a$.

Boundary conditions on the supercurrents [171] produce vortices to be perpendicular to the vacuum–superconductor interface within a thickness of the order of penetration depth at the temperature at which the surface pinning is effective, $\lambda(T_i) \sim 0.4$ μm ($T_i/T_c \sim 0.92$ for $B \sim 30$ G [88]). For samples with $t \lesssim 2\lambda(T_i) \sim 0.8$ μm the square VS will be
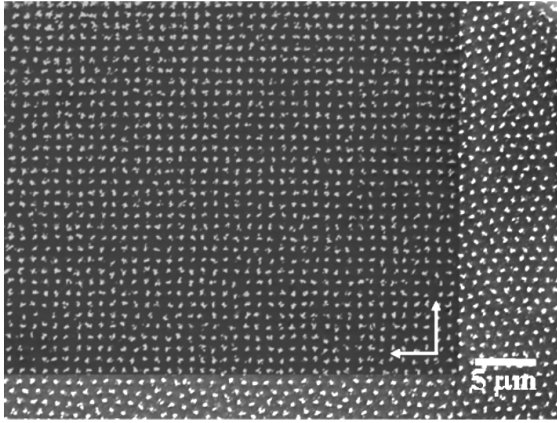
Figure 17. Magnetic-decoration image of the bottom-surface $Bi_2Sr_2CaCu_2O_8$ vortex structure for a thickness of (0.5 ± 0.3) μm. The region with darker background is located beneath the top-surface square array of dots. Arrows depict the [10] and [01] directions of the pinning pattern. Reprinted from [89] with permission from Elsevier.

stable at the top surface only if the concomitant increment in interaction energy is compensated by a pinning-energy gain. Therefore the effective pinning energy per Fe dot and per vortex can be estimated as $E_p = E_{int}^{sq} - E_{int}^{hex}$, where E_{int}^{sq} is the interaction energy accumulated in the propagation volume and E_{int}^{hex} that of the hexagonal structure that would be stable in the same volume if no surface pinning were present. In first approximation $E_{int}^{sq} \sim t_{pr}\epsilon_{int}^{sq}$, with ϵ_{int}^{sq} the interaction energy per unit length of the square VS imaged for $t = (0.5 \pm 0.3)$ μm. The term E_{int}^{hex} can be obtained from the hexagonal VS that is stable in pristine regions. Assuming $t_{pr} \sim 1$ μm, the effective pinning energy can be estimated as $E_p \sim 7 \times 10^{-13}$ erg, which gives $\epsilon_p = E_p/t_{pr} = 0.007\epsilon_0$. This indicates that the surface pinning is weak: it has the same magnitude as the pinning

associated with a cylindrical hole of diameter ξ and length 600 Å $\sim 0.06t_{pr}$.

The microscopic structural properties of the interface were studied at the bottom surface of several patterned regions for two thicknesses, (2.5 ± 0.3) and (3.5 ± 0.3) μm. Figure 18 shows a typical magnetic-decoration image of the bottom-surface VS for $t = (3.5 \pm 0.3)$ μm. The structure presents square-symmetry domains and hexagonal unit cells with area-preserving rhombohedral distortions. Statistics in 15 000 unit cells for $t = (2.5 \pm 0.3)$ μm and (3.5 ± 0.3) μm reveal that 17% of vortices belong to square-symmetry domains with an average lattice parameter equal to that of the pinning structure, a_{sq}. From the rest, 71% of vortices belong to hexagonal domains with rhombohedral distortions along either the [10] or [01] principal directions of the surface pinning; see the upper panel of figure 18. A small fraction of vortices, 12%, belong to hexagonal domains distorted along an arbitrary direction. These regions might have origin on the stress relaxation between square and distorted-hexagonal domains.

The proportion of vortices belonging to square or distorted-hexagonal domains is roughly the same (within 3%) for the interface observed at $t = (2.5\pm0.3)$ and (3.5 ± 0.3) μm. The location of square-symmetry domains is uncorrelated for both thicknesses, as illustrated in the example of figure 19. This implies that the particular location of square-symmetry domains is not associated with spatial inhomogeneities in the surface pinning. This result, and the similar number of vortices belonging to square-symmetry domains for both thicknesses, suggest that the interface observed at the bottom surface of the sample is representative of that generated at the interior of thicker samples ($t > 3.5$ μm). Further studies are necessary in order to fully confirm this indication. Experimentally, this constitutes an important challenge since most of the real-space imaging techniques have access to the VS only at the sample surface.
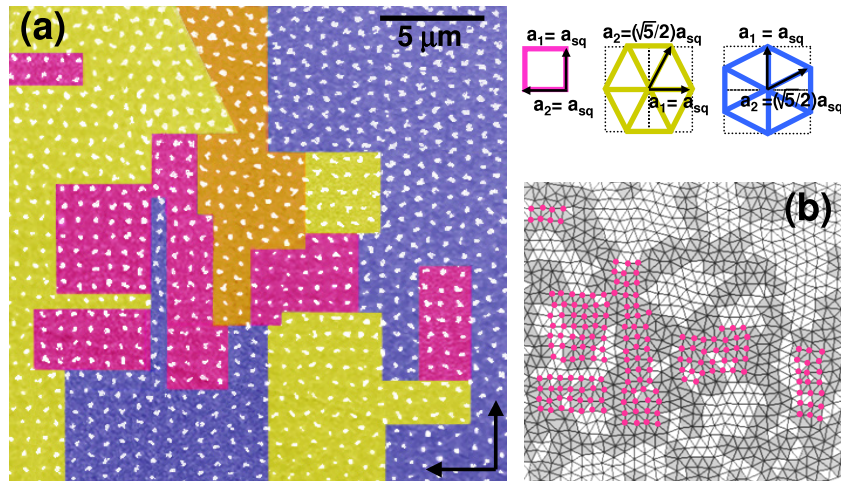
Figure 18. Magnetic-decoration image of the bottom-surface $Bi_2Sr_2CaCu_2O_8$ vortex structure for a thickness of (3.5 ± 0.3) μm. All vortices in the image are located beneath a top-surface patterned area. (a) Vortices arrange in domains with square (black/magenta) and distorted-hexagonal (light grey/yellow, dark grey/blue and grey/orange) symmetries. Arrows indicate the [10] and [01] directions of the pinning structure. Upper panel: schematics of the unit cells of the different domains and of the rhombohedral distortion of the hexagonal polytype along the [10] and [01] axes of the square pinning. Reprinted from [89] with permission from Elsevier. (b) Delaunay triangulation of the vortex structure, where topological defects of the hexagonal structure are highlighted in grey. The vortices belonging to square-symmetry domains are indicated with the black/magenta dots.
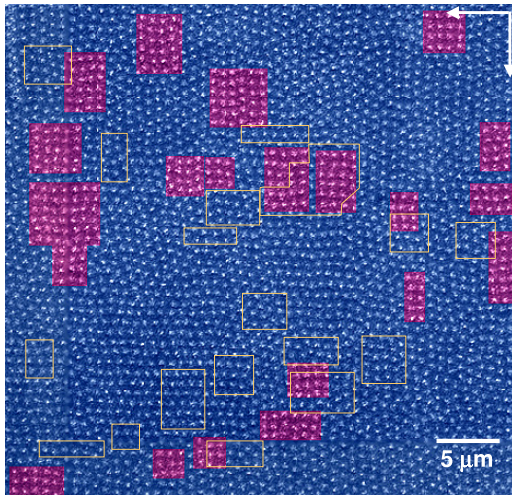
Figure 19. Location of square-symmetry domains of the bottom-surface $Bi_2Sr_2CaCu_2O_8$ vortex structure for thicknesses of (2.5 ± 0.3) and (3.5 ± 0.3) μm. Magnetic-decoration image: vortex structure beneath the square pinning for $t = 3.5$ μm; square-symmetry domains depicted in black (magenta online). White (yellow) frames: location of the square-symmetry domains observed in the experiment with $t = 2.5$ μm. Reprinted from [89] with permission from Elsevier.

Within our experimental resolution of $0.02a$ the average unit-cell areas of square and distorted-hexagonal domains are equal to those of the top-surface square VS and of the bottom-surface hexagonal VS observed in thick samples. Therefore the square-to-hexagonal transition proceeds along the direction of vortices via an area-preserving transformation path. Magnetic-decoration imaging of this transformation probes the structural properties of interfaces formed in symmetry-change phase transitions when keeping the volume constant. To our knowledge this is the first experiment that provided direct insight into this phenomenon with microscopic resolution.

In condensed matter physics, square-to-hexagonal phase transitions are typically of first order [172, 173]. Since in this transformation one of the phases is not a subgroup of the space group of the other, the conventional continuous Ginzburg–Landau theory of phase transitions does not properly describe all the possible transition paths [172, 173]. Several transformation paths of the square-to-hexagonal transition have been theoretically studied [172–175] for different magnitudes of the strain energy stored in the transformation. In principle, a hexagonal structure can transform into a square along the direction of vortices in a continuous way, i.e. performing only shear deformations. For example, the simulations of [175] indicate that the ground-state transition path encompasses the formation of a large-cell superstructure (more than 20 vortices per unit cell) where every vortex in a cell has a non-equivalent displacement produced by shear deformations. The collective displacement of vortices involved in this continuous transformation path will produce a macroscopic deformation of the vortex structure being elongated in the direction of the deformation and compressed in the perpendicular one. It is also theoretically proposed that other non-continuous transition paths encompassing simpler transformations or the formation

of domains have an energy similar to that of the ground state [174, 175].

In the particular case studied here, the $Bi_2Sr_2CaCu_2O_8$ vortex structure transforms from square to hexagonal through the formation of an interface where domains with square and hexagonally distorted symmetries coexist. This coexistence leads to the nucleation of an important fraction of edge dislocations (plastic deformations), mainly at the boundaries of the domains. This is revealed by the Delaunay triangulation of the interface structure shown in figure 18(b). Therefore, in the square-to-hexagonal structural transformation observed in $Bi_2Sr_2CaCu_2O_8$, plastic deformations of the VS play a relevant role. As we will discuss below, the layered nature of the $Bi_2Sr_2CaCu_2O_8$ VS that affects the nucleation and growth of the vortex solid can favour the nucleation of defects in this non-continuous transition path.

Other reasons might not favour a continuous transition path in this case. First, the macroscopic deformation of the VS resulting from a continuous transition path [173, 175] is not energetically favourable since the square vortex structure is only stable in a confined region of the sample of roughly 50×50 μm^2. Partly as a consequence of this, if other transition paths with similar energies are available, it is very likely that the system will choose a metastable non-continuous path encompassing a simpler transformation or eventually the formation of domains. This situation can be boosted by the presence of quenched disorder such as that associated to the bulk pinning potential when field cooling the vortex structure [175]. Molecular-dynamics studies [174] inspired by our results in $Bi_2Sr_2CaCu_2O_8$ support these arguments.

These simulations were performed by fixing vortex positions at the patterned surface, i.e. the surface pinning was considered infinite. Taking into account a model of rigid vortices where the line energy competes with the vortex–vortex interaction energy, the vortex positions at the bottom surface were obtained as a function of the sample thickness [174, 175]. Within this model, at zero temperature the ground state of the square-to-hexagonal transition does not entail the formation of an interface, but instead a continuous transition path is found [174]. However, the effect of a finite temperature results in a discontinuous transformation path that encompasses the coexistence of domains with distorted-hexagonal and square symmetries at the interior of the sample. The authors propose [174, 175] that the interface observed in our experiments is a metastable state that stems from a quenching of this domain-like structure [174]. This is quite likely since the magnetic decorations were performed at low temperatures after field cooling from $T > T_i \sim T_m$ [32, 41]. Nevertheless, in order to quantitatively compare these findings with the experimental results, simulations should consider more realistic conditions. For example, the elastic and anisotropic nature of vortices, the finite magnitude of the superficial pinning and the supercurrents' boundary conditions should be taken into account.

As mentioned, a transition path encompassing plastic deformations can be promoted by the nucleation and growth mechanisms of the vortex solid in an extremely anisotropic high-T_c material such as $Bi_2Sr_2CaCu_2O_8$. Theoretical [176, 177] and experimental [178] results suggest that in

this material the superconducting phase coherence is induced by Josephson coupling between pancake vortices (PVs) nucleated in the Cu–O$_2$ planes. The vortex liquid phase is composed of decoupled PVs that transform into a solid of vortex lines when cooling below the melting temperature [14, 15]. This liquid–solid phase transition [32, 33] is a result of a collective response of PVs to the competition between thermal, vortex–vortex and vortex-pinning interaction energies. At T_m the thermal energy balances the other two contributions. As we already mentioned in section 4.2, when field cooling the sample below $T_i \sim T_m$ [32, 41] the bulk pinning becomes effective and the vortex structure remains frozen at lengthscales of a [136, 154]. In this way, the low-field vortex structure nucleated at $T_i \sim T_m$ [32, 41] is preserved when performing magnetic decorations at low temperatures [78].

The results presented in this section indicate that when cooling through $T_i \sim T_m$ [32, 41] the sites of the square surface pinning act as nucleation centres for the three-dimensional vortex solid. The weak interaction between vortices at these low fields and high temperatures allows the propagation of a square VS down to a distance of at least the range of the magnetic pinning, $\lambda(T_m) \sim 0.4~\mu$m for Bi$_2Sr_2$CaCu$_2O_8$. When the accumulated interaction energy is no longer compensated by the surface-pinning energy, the interface shown in figure 18 is generated. At the interface, the edge dislocations are produced via significant displacements of the PVs of adjacent planes. Since the Bi$_2$Sr$_2$CaCu$_2$O$_8$ vortex matter is extremely anisotropic, these displacements entail an energetic cost that can be accounted by the weak-pinning energy gain [176, 177]. Therefore, the extremely anisotropic nature of Bi$_2$Sr$_2$CaCu$_2$O$_8$ vortex matter promotes the plastic deformations observed in this non-continuous square-to-hexagonal transition path.

6. Vortex structural transitions involving elastic deformations: the case of NbSe$_2$

In contrast to the case of Bi$_2$Sr$_2$CaCu$_2$O$_8$, the field-cooled NbSe$_2$ vortex structure is polycrystalline [78, 79]. Figure 20(a) shows a typical FC magnetic-decoration image obtained at low fields. This polycrystal is obtained due to the particular nucleation and growth mechanisms of the NbSe$_2$ vortex structure [46]. On field cooling through $T_{c2}(H)$, the nucleation of the vortex solid occurs concomitantly with the normal–superconductor phase transition. At this temperature, the vortex–vortex interaction energy is important and therefore small crystallites start to nucleate. On slight cooling, the growth of crystallites is inhibited at $T_i \lesssim T_{c2}$ [8, 155, 156] ($T_i \sim 0.99T_{c2}$ for 40 G [156]). This is due to an effective viscosity associated with the setting in of bulk pinning, resulting in a polycrystalline vortex structure. On further cooling down to 4 K, in order to profit from pinning, vortices will displace distances of the order of ξ, that in NbSe$_2$ is only a small fraction of a (for the typical values of $B < 100$ G in decoration experiments). Therefore, the low-temperature structure will remain polycrystalline [46]. For further details about this discussion we refer the reader to [46].
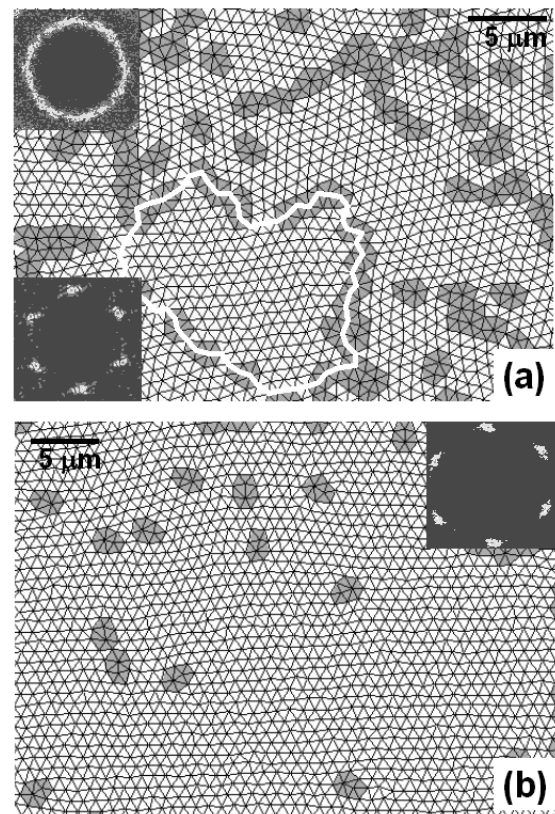
Figure 20. Crystallization of the NbSe$_2$ vortex structure by a dynamical ordering method. (a) Typical polycrystalline VS obtained in a FC experiment. Insets: Fourier transform considering the vortices from the whole image (top) and from inside the grain contoured in white (bottom). (b) Typical single-crystalline VS obtained after quenching the dynamically ordered state (FCR experiment; see text). Inset: Fourier transform considering all vortices. In both cases the magnetic induction $B = 36$ G.

The first attempt to induce a structural symmetry transition in NbSe$_2$ vortex matter consisted in nucleating the FC structure in the presence of a perfectly hexagonal pinning structure [179]. The result was the formation of Moiré patterns and regions where vortices match the pinning structure. The proportion of these two types of domains is the same as in Bitter pinning experiments (70% of vortices in Moiré domains) [179]. This result indicates that the surface pinning is not effective enough to induce a local rigid rotation of the crystallites of the polycrystalline FC vortex structure.

Considering the previous evidence, changing the symmetry of the pinning structure from hexagonal to square will not significantly alter the result in FC experiments. As a consequence, a different experimental approach was considered. In previous works [78, 180, 181] a single-crystalline NbSe$_2$ vortex structure was induced by means of a dynamical-ordering method. These experiments were inspired by the theoretical prediction [182] that the disordered VS, when driven at high velocities, undergoes a dynamical crystallization. Therefore, in this process the VS 'loses memory' of the effect of the random bulk pinning. The particular experimental realization considered in our work consists in quenching the dynamically ordered
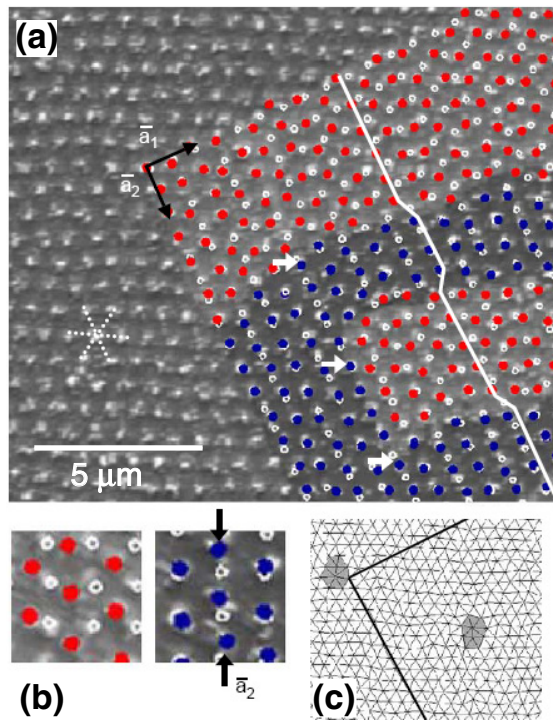
Figure 21. NbSe$_2$ vortex structure interacting with a square surface pinning in the first matching condition ($B = 32.6$ G). (a) Magnetic-decoration image of the field-cooled vortex structure nucleated in pristine and patterned regions. Dotted lines depict the compact planes of the hexagonal structure in the pristine region; arrows indicate the principal directions of the square pinning. In the patterned region pinning sites are indicated with white open circles and vortices are highlighted in colours. The light-background areas are floating-hexagonal domains (white (red online) vortices) whereas the dark-background areas are distorted-hexagonal domains (dark (blue) vortices). (b) Enlarged images of the floating-hexagonal (left) and distorted-hexagonal (right) domains. Black arrows indicate the direction of the rhombohedral distortion. (c) Delaunay triangulation of the VS; the frame indicates the edge of the patterned area. Reprinted from [101] with permission from Elsevier.

VS induced after driving vortices with currents much larger than the critical. Details of this FCR (field-cooling-rotated) method can be found in [78]. A typical decoration image of the single-crystalline FCR NbSe$_2$ vortex structure is shown in figure 20(b).

In the following experiments, the NbSe$_2$ vortex structure was field-cooled in a sample with square arrays of Fe dots and then dynamically ordered at 4.2 K. The periodic pinning consisted in a structure of Fe dots with $a_{sq} = 0.8$ μm and $R_D = 0.13$ μm. The VS was nucleated at the first matching field ($B = 32.6$ G). As an example, figure 21 shows a typical magnetic-decoration image of the FCR NbSe$_2$ vortex structure in the vicinity of the square pinning pattern [101, 179]. The VS was dynamically ordered in order to have one of its compact planes parallel to a principal direction of the square pinning. In patterned regions an alternation of floating- and distorted-hexagonal domains is observed; see figure 21. This is in contrast with the square VS induced in patterned areas of Bi$_2$Sr$_2$CaCu$_2$O$_8$ crystals.

The floating-hexagonal domains correspond to an isotropic hexagonal VS that is insensitive to the position of pinning sites and parallel to the VS nucleated in pristine regions. In the distorted-hexagonal domains an area-preserving rhombohedral deformation compresses vortices along the [10] or [01] directions of the pinning structure. In these domains half of vortices are pinned by the Fe dots: in one compact plane they match the pinning sites and in the adjacent plane vortices are located in between dots; see figure 21. Besides, for every compact plane parallel to the axis of the rhombohedral deformation, a superstructure of vortices alternating on top of and in between dots is observed; see the white arrows in figure 21(a). This allows the relaxation of the stress that would be generated if all vortices in a compact plane were on top of pinning sites.

The observation of the floating-hexagonal domains could be attributed to spatial variations in the magnitude of the surface pinning. However, throughout the whole patterned region there is an alternation of 5–6 unit cells of the floating-hexagonal domain with 3–4 unit cells of the distorted-hexagonal domain. The existence of this superstructure is a strong indication that both domains have an intrinsic and interdependent origin and therefore do not stem from spatial variations of the surface pinning. This is also supported by the zigzagging of vortex compact planes between both domains: in the floating-hexagonal regions they are placed in between rows of pinning sites while in the distorted-hexagonal domains run on top of pinning-site rows. This is indicated in figure 21 with a white line.

At the bottom surface of thick samples the alternation of distorted-hexagonal and floating-hexagonal domains is energetically unstable, and therefore an isotropic hexagonal VS will be recovered. In connection with this, it is important to note that the interconnection between the hexagonal-distorted and floating domains of the top surface proceeds elastically. The absence of grain boundaries is shown in the Delaunay triangulation of figure 21(c). This result suggests that the symmetry transition from the top-surface-distorted-hexagonal to the bottom-surface-isotropic-hexagonal structure is accomplished via elastic deformations along the direction of vortices.

The latter is further supported by the quantitative agreement with results obtained with a simple elastic model [179]. At the bottom surface, an isotropic hexagonal vortex lattice with one of its compact planes parallel to a principal direction of the top-surface square pinning is assumed. The model takes into account the transversal distance between the position of a vortex at the bottom surface and that of the closest pinning site at the top surface, u_t. The location of each vortex at the top surface is determined by comparing u_t with the pinning range of the magnetic dots, considered as $r_p \approx R_D + \lambda(4.2$ K$) \approx 0.3a_{hex}$. When u_t is smaller than the pinning range, at the top-surface vortices occupy the dots, stabilizing the distorted-hexagonal domains. If $u_t \geqslant r_p$ vortices do not profit from the top-surface pinning sites and the distorted-hexagonal structure is unstable. The elastic strain along the direction of vortices is therefore relaxed stabilizing the floating-hexagonal structure. When vortex positions at the bottom surface are again displaced less
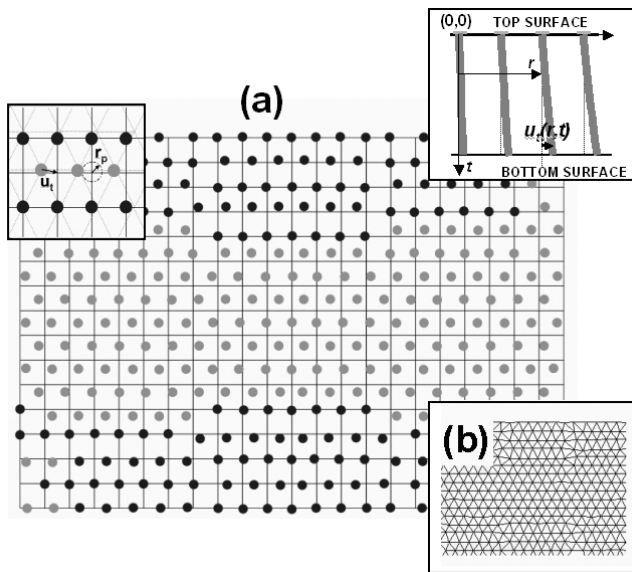
Figure 22. Elastic model that accounts for the observed alternation of floating- and distorted-hexagonal domains in the NbSe$_2$ VS nucleated in a region with square surface pinning. (a) Pinning sites (corners of the square grid) and vortex positions (full circles) at the top surface. Vortices belonging to floating- and distorted-hexagonal domains are depicted in grey and dark grey, respectively. Reproduced from [100] with kind permission of Springer Science and Business Media. Insets: top (left) and lateral (right) view of vortex displacements, $u_t(r)$, and range of the magnetic pinning, r_p. (b) Delaunay triangulation of the top-surface vortex structure: the in-plane transition between floating- and distorted-hexagonal domains is accomplished elastically.

than r_p from pinning sites, distorted-hexagonal domains are stabilized. A sketch of this model is presented in figure 22. The quantitative agreement between the alternation period of floating- and distorted-hexagonal domains obtained with this model and the one observed experimentally strongly supports the structural transition induced in NbSe$_2$ being produced via elastic deformations. Therefore, the moderately anisotropic nature of NbSe$_2$ vortex matter inhibits a structural change involving plastic deformations such as the one observed in Bi$_2$Sr$_2$CaCu$_2$O$_8$.

This can be further supported by comparatively analysing the elastic response of NbSe$_2$ and Bi$_2$Sr$_2$CaCu$_2$O$_8$ vortex matter to the short-wavelength (high-k_z) perturbation introduced by the top-surface pinning. In the low-field regime investigated here, compression and shear moduli are small in comparison to the tilt modulus [7]. Besides, the individual-vortex term of c_{44} dominates over the lattice contribution. Therefore, the propagation process of the structural transition induced at the surface is mainly determined by the individual-vortex elastic properties.

Considering this, and the dependence of c_{44} on k_z shown in figure 1, it is clear that the VS response for high k_z is significantly more dispersive in Bi$_2$Sr$_2$CaCu$_2$O$_8$ than in NbSe$_2$. Consequently, the longitudinal propagation length of a locally induced structural transition will be greater in NbSe$_2$ than in Bi$_2$Sr$_2$CaCu$_2$O$_8$ [101], implying a higher interaction-energy cost. If the energy gained when profiting from pinning sites

cannot account for this cost, then the matching between both structures is not likely. This seems to be the case in NbSe$_2$ vortex matter: instead of matching the sites of the square top-surface pattern, the pinning is partially profited in order to decrease the strain energy along the propagation length of the transformation. This is a consequence of the extreme sensitivity of the VS elastic properties to the anisotropy of the superconducting parameters.

7. Conclusions and perspectives

The experiments discussed in this review illustrate that the magnetic-decoration technique can provide a wealth of information in the phenomenology of vortex structural transitions. This is a consequence of the wide range of fields in which individual vortices can be directly imaged spanning macroscopic regions of the sample. In particular, the experiments detailed in sections 5 and 6 explored the role played by substrate disorder, nucleation and growth dynamics of the vortex solid, elastic properties and anisotropy of vortex matter.

The results obtained in the two examples presented indicate that the response of vortex matter to perturbations along the direction of vortices is mainly dominated by the tilting energy of individual vortices. This magnitude determines whether or not a non-hexagonal VS can be induced and stabilized in a finite volume by means of a surface-pinning potential. Although the dispersive nature of c_{44} produces a softening of vortex matter, anisotropy plays a decisive role in the nature of the symmetry transition induced along the direction of vortices. In the case of extremely anisotropic vortex matter, the energy required to produce a significant displacement of PVs of adjacent planes can be compensated by even a weak surface-pinning potential. Therefore such displacements promote a symmetry-change transition through a transformation path encompassing plastic deformations. In contrast, in moderately anisotropic vortex matter as in the case of NbSe$_2$, plastic deformations are energetically much more expensive and the system undergoes a structural transition performing only elastic deformations. In this case, the partial profit of pinning is justified by the inherent decrease of strain energy accumulated along the direction of vortices.

Although the response of Bi$_2$Sr$_2$CaCu$_2$O$_8$ and NbSe$_2$ vortex matter to the presence of the same surface-pinning potential is radically different, they have similar topological characteristics when nucleated in pristine regions. This indicates that the different dimensionality of vortices in both materials is revealed when introducing surface-pinning structures that produce short-wavelength perturbations.

In spite of the considerable amount of results on imaging structural transitions induced in vortex matter, many open issues still remain. For example, the fact that when nucleating the vortex structure in the presence of a square pinning potential the effect of random bulk pinning is less important than in the case of a hexagonal pinning might have interesting implications. One plausible explanation could be that the square pinning potential increases the melting temperature of an elastic system with respect to a hexagonal

one. This question can be addressed by studying the surface melting transition of the VS with local-magnetization sensitive techniques, such as scanning Hall probe microscopy [183] or differential magneto-optics [184].

Since most of the techniques that directly image structural transitions are sensitive to the location of vortices at the sample surface, an important aspect that remains barely studied is if the structure observed at the surface of a thin sample is representative of the one that is stable in the interior of a thick sample. In the case of the structural transition discussed in section 5, the thickness independence of the proportion of vortices in square and distorted-hexagonal domains was considered as a strong indication that the interface observed in thin samples is representative of that found in the interior of thick samples. Numerical simulations with realistic boundary conditions would be of great help in order to fully confirm this suggestion. From the experimental point of view, Lorentz microscopy is, up to this moment, the only technique that allows the direct imaging of the VS inside the material [185, 186]. The thickest samples that can be studied with state-of-the-art Lorentz microscopes have a thickness of approximately 0.4 μm [185, 186]. Therefore the application of this technique to the study of structural transitions in the interior of samples is quite limited, and this problem remains a challenging experimental issue.

In conclusion, the magnetic-decoration technique has not only a venerable history but a promising future to continue to unveil the real-space microscopic details of structural transitions induced in vortex matter.

Acknowledgments

References

[1] Blatter G, Feigel'man M V, Geshkenbein V B, Larkin A I and Vinokur V M 1994 *Rev. Mod. Phys.* **66** 1125

[2] Cava R J, Batlogg B, Krajewski J, Peck W F Jr, Mizuhashi K, Lee J O, Eisaki H, Takagi H and Uchida S 1994 *Phys. Rev.* B **50** 647

[3] Ramirez A P, Huse D A, Bishop D J, Goldman A I, Stassis C, Canfield P C, Mortensen K, Yaron U, Gammel P L and Eskildsen M R 1996 *Nature* **382** 236

[4] Essmann U and Träuble H 1967 *Phys. Lett.* A **24** 526

[5] Tinkham M 1996 *Introduction to superconductivity* 2nd edn (New York: McGraw-Hill)

[6] Yao Z, Yoon S, Dai H, Fan S and Lieber C 1994 *Nature* **371** 777

[7] Yoon S, Yao Z, Dai H and Lieber C 1995 *Science* **270** 270

[8] Marchevsky M, Keurentjes A, Kes P H and Aarts J 1998 *Phys. Rev.* B **57** 6061

[9] Nelson D R 1992 *Phenomenology and Applications of High-Temperature Superconductors* vol 187 (New York: Addison-Wesley)

[10] Marchetti M C and Nelson D R 1993 *Phys. Rev.* B **47** 12214

[11] Kogan V G 1981 *Phys. Rev.* B **24** 1572

[12] Hess H F, Murray C A and Waszczak J V 1992 *Phys. Rev. Lett.* **69** 2138

[13] Lawrence W E and Doniach S 1971 *Proc. 12th Int. Conf. on Low Temperature Physics* vol 361

[14] Matsuda Y, Gaifullin M B, Kumagai K, Kosugi M and Hirata K 1997 *Phys. Rev. Lett.* **78** 1972

[15] Colson S, Konczykowski M, Gaifullin M B, Matsuda Y, Gierlowski P, Li M, Kes P H and van der Beek C J 2003 *Phys. Rev. Lett.* **90** 137002

[16] Josephson B D 1962 *Phys. Lett.* **1** 251

[17] Abrikosov A A 1957 *Zh. Eksp. Teor. Fiz.* **32** 1442

[18] Larkin A I 1970 *Sov. Phys.—JETP* **31** 784

[19] Nattermann T 1990 *Phys. Rev. Lett.* **64** 2454

[20] Giamarchi T and Le Doussal P 1994 *Phys. Rev. Lett.* **72** 1530

[21] Giamarchi T and Le Doussal P 1995 *Phys. Rev.* B **52** 1242

[22] Marchevsky M V 1995 *PhD Thesis* Leiden University, Leiden

[23] Kim P, Yao Z, Bolle C A and Lieber C 1999 *Phys. Rev.* B **60** R12589

[24] Klein T, Joumard I, Blanchard S, Marcus J, Cubitt R, Giamarchi T and Le Doussal P 2001 *Nature* **413** 404

[25] Fasano Y, De Seta M, Menghini M, Pastoriza H and de la Cruz F 2005 *Proc. Natl. Acad. Sci. USA* **102** 3898

[26] Giamarchi T and Bhattacharya S 2002 *High Magnetic Fields Applications in Condensed Matter Physics and Spectroscopy* vol 314 (Berlin: Springer)

[27] Fisher D S 1997 *Phys. Rev. Lett.* **78** 1964

[28] Kierfeld J, Nattermann T and Hwa T 1997 *Phys. Rev.* B **55** 626

[29] Nelson D R 1988 *Phys. Rev. Lett.* **60** 1973

[30] Gammel P L, Schneemeyer L F and Bishop D J 1991 *Phys. Rev. Lett.* **66** 953

[31] Safar H, Gammel P L, Huse D A, Bishop D J, Rice J P and Ginsberg D M 1992 *Phys. Rev. Lett.* **69** 824

[32] Pastoriza H, Goffman M F, Arribere A and de la Cruz F 1994 *Phys. Rev. Lett.* **72** 2951

[33] Zeldov E, Majer D, Konczykowski M, Geshkenbein V B, Vinokur V M and Shtrikman H 1995 *Nature* **375** 373

[34] Schilling A, Fisher R A, Phillips N E, Welp U, Dasgupta D, Kwok W K and Crabtree G W 1996 *Nature* **382** 791

[35] Fisher D S, Fisher M P A and Huse D A 1991 *Phys. Rev.* B **43** 130

[36] Cubitt R *et al* 1993 *Nature* **365** 407

[37] Zeldov E, Majer D, Konczykowski M, Larkin A I, Vinokur V M, Geshkenbein V B, Chikumoto N and Shtrikman H 1995 *Europhys. Lett* **30** 367

[38] Khaykovich B, Zeldov E, Majer D, Li T W, Kes P H and Konczykowski M 1996 *Phys. Rev. Lett.* **76** 2575

[39] Avraham N *et al* 2001 *Nature* **411** 451

[40] Khaykovich B, Konczykowski M, Zeldov E, Doyle R A, Majer D, Kes P H and Li T W 1997 *Phys. Rev.* B **56** R517

[41] Goffman M F, Herbsommer J A, de la Cruz F, Li T W and Kes P H 1998 *Phys. Rev.* B **57** 3663

[42] Paltiel Y *et al* 2000 *Phys. Rev. Lett.* **85** 3712

[43] Paltiel Y, Zeldov E, Myasoedov Y, Shtrikman H, Bhattacharya S, Higgins M J, Xiao Z L, Andrei E Y, Gammel P L and Bishop D J 2000 *Nature* **403** 398

[44] Angurel L A, Amin F, Polichetti M, Aarts J and Kes P H 1997 *Phys. Rev.* B **56** 3425

[45] Ling X S, Park S R, McClain B A, Choi S M, Dender D C and Lynn J W 2001 *Phys. Rev. Lett.* **86** 712

[46] Fasano Y, Menghini M, de la Cruz F, Paltiel Y, Myasoedov Y, Zeldov E, Higgins M J and Battacharya S 2002 *Phys. Rev.* B **66** R020512

[47] Menghini M, Fasano Y and de la Cruz F 2002 *Phys. Rev.* B **65** 064510

[48] Nelson D R and Vinokur V M 1992 *Phys. Rev. Lett.* **68** 2398

[49] Nelson D R and Vinokur V M 1993 *Phys. Rev.* B **48** 13060

[50] Osquiguil E, Balseiro C, Nieva G, Grigera S A, Morre E and de la Cruz F 1998 *Phys. Rev. Lett.* **81** 2348

[51] Daldini O, Martinoli P, Olsen J L and Berner G 1974 *Phys. Rev. Lett.* **32** 218

[52] Fiory A T, Hebard A F and Somekh S 1978 *Appl. Phys. Lett.* **32** 73

[53] Otani Y, Pannetier B, Nozières J P and Givord D 1993 *J. Magn. Magn. Mater.* **126** 622

[54] Martín J I, Vélez M, Nogués J, Schuller I K and Vicent J L 1997 *Phys. Rev. Lett.* **79** 1929

[55] Morgan D J and Ketterson J B 1998 *Phys. Rev. Lett.* **80** 3614

[56] Martín J I, Vélez M, Hoffmann A, Schuller I K and Vicent J L 2000 *Phys. Rev.* B **62** 9110

[57] Fiory A T, Hebard A F and Somekh S 1977 *IEEE Trans. Magn.* **13** 589

[58] Baert M, Metlushko V V, JonckHeere R, Moshchalkov V V and Bruynseraede Y 1995 *Phys. Rev. Lett.* **74** 3269

[59] Bezryadin A and Pannetier B 1995 *J. Low Temp. Phys.* **98** 251

[60] Moshchalkov V V, Baert M, Metlushko V V, Rosseel E, Van Bael M J, Temst K and Bruynseraede Y 1998 *Phys. Rev.* B **57** 3615

[61] Metlushko V V *et al* 2003 *Appl. Phys. Lett.* **83** 4217

[62] Hallen H D, Seshadri R, Chang A M, Miller R E, Pfeiffer L N, West K W and Murray C A 1993 *Phys. Rev. Lett.* **71** 3007

[63] Runge K and Pannetier B 1993 *Europhys. Lett.* **24** 737

[64] Matsuda T, Harada K, Kasai H, Kamimura O and Tonomura A 1996 *Science* **271** 1393

[65] Martín J I, Nogués J, Liu K, Vicent J L and Schuller I K 2003 *J. Magn. Magn. Matter.* **256** 449

[66] Reichhardt C, Olson C J, Grønbech-Jensen N and Nori F 2001 *Phys. Rev. Lett.* **86** 4354

[67] Scalettar R T, Hoffmann A, Reichhardt C, Zimanyi G T and Schuller I K 2001 *Phys. Rev.* B **64** 052503

[68] Jaccard Y, Martin J I, Cyrille M C, Velez M, Vicent J L and Schuller I K 1998 *Phys. Rev.* B **58** 8232

[69] Hoffmann A, Schuller I K, Martin J I, Velez M and Vicent J L 1999 *Phys. Rev. Lett.* **83** 1022

[70] Terentiev A, Cooley L D, Morgan D J, Ketterson J B, Watkins D B and De Long L E 2000 *Phys. Rev.* B **61** R9249

[71] Hoffmann A, Prieto P and Schuller I K 2000 *Phys. Rev.* B **61** 6958

[72] Silevitch D M, Reich D H, Chien C L, Field S B and Shtrikman H 2001 *J. Appl. Phys.* **89** 7478

[73] Van Bael M J, Temst K, Moshchalkov V V and Bruynseraede Y 1999 *Phys. Rev.* B **59** 14674

[74] Leghissa M, Gurevich L A, Kraus M, Saemann-Ischenko G and Vinnikov L Ya 1993 *Phys. Rev.* B **48** 1341

[75] Dai H, Yoon S, Liu J, Budhani R C and Lieber C M 1994 *Science* **265** 1552

[76] Harada K, Kamimura O, Kasai H, Matsuda T, Tonomura A and Moshchalkov V V 1996 *Science* **274** 5290

[77] Bezryadin A, Ovchinnikov Yu N and Pannetier B 1996 *Phys. Rev.* B **53** 8553

[78] Fasano Y, Herbsommer J A, de la Cruz F, Pardo F, Gammel P L, Bucher E and Bishop D J 1999 *Phys. Rev.* B **60** 15047

[79] Fasano Y, Herbsommer J A and de la Cruz F 1999 *Phys. Status Solidi* b **215** 563

[80] van Bael M J, Bekaert J, Temst K, Van Look L, Moshchalkov V V, Bruynseraede Y, Howells G D, Grigorenko A N, Bending S J and Borghs G 1999 *Phys. Rev. Lett.* **86** 155

[81] Fasano Y, Menghini M, Nieva G and de la Cruz F 2000 *Phys. Rev.* B **62** 15183

[82] Grigorenko A N *et al* 2000 *Physica* C **332** 20

[83] Bending S J *et al* 2001 *Phys. Rev.* B **63** 052504

[84] Surdeanu R, Wijngaarden R J, Griessen R, Einfeld J and Wördenweber R 2001 *Europhys. Lett.* **54** 682

[85] Van Bael M J, Lange M, Raedts S, Moshchalkov V V, Grigorenko A N and Bending S J 2003 *Phys. Rev.* B **68** 014509

[86] Field S B, James S S, Barentine J, Metlushko V, Crabtree G, Shtrikman H, Ilic B and Brueck S R J 2002 *Phys. Rev. Lett.* **88** 067003

[87] Van Bael M J, Lange M, Moshchalkov V V, Fangohr H, deGroot P A J, Grigorenko A N and Bending S J 2003 *Phys. Rev. Lett.* **90** 237001

[88] Menghini M, Fasano Y, de la Cruz F, Banerjee S S, Myasoedov Y, Zeldov E, van der Beek C J, Konczykowski M and Tamegai T 2003 *Phys. Rev. Lett.* **90** 147001

[89] Fasano Y, de Seta M, Menghini M, Pastoriza H and de la Cruz F 2003 *Solid. State Commun.* **128** 51

[90] Fasano Y, de Seta M, Menghini M, Pastoriza H and de la Cruz F 2004 *Physica* C **408–410** 520

[91] Veauvy C, Hasselbach K and Mailly D 2004 *Phys. Rev.* B **70** 214513

[92] Karapetrov G, Fedor J, Iavarone M, Rosenmann D and Kwok W K 2005 *Phys. Rev. Lett.* **95** 167002

[93] Björnsson P G, Maeno Y, Huber M E and Moler K A 2005 *Phys. Rev.* B **72** 012504

[94] Reichhardt C, Olson C J and Nori F 1998 *Phys. Rev.* B **58** 6534

[95] Yurchenko V V, Wördenweber R, Galperin Yu M, Shantsev D V, Vestgarden J I and Johansen T H 2006 *Physica* C **437/438** 357

[96] Tonomura A 2005 *Proc. Natl. Acad. Sci. USA* **102** 14952

[97] Civale L, Marwick A D, Worthington T K, Kirk M A, Thompson J R, Krusin-Elbaum L, Sun Y, Clem J R and Holtzberg F 1991 *Phys. Rev. Lett.* **67** 648

[98] Laguna M F, Cornaglia P S and Balseiro C A 2002 *Phys. Rev.* B **66** 024522

[99] Fasano Y, Menghini M and de la Cruz F 2004 *Physica* C **408–410** 474

[100] Fasano Y, De Seta M, Menghini M, Pastoriza H and de la Cruz F 2004 *J. Low Temp. Phys.* **135** 99

[101] Fasano Y, De Seta M, Menghini M, Pastoriza H and de la Cruz F 2006 *J. Phys. Chem. Solids* **67** 395

[102] Hess H F, Robinson R B, Dynes R C, Valles J M Jr and Waszczak J V 1989 *Phys. Rev. Lett.* **62** 214

[103] Troyanovski A M, Aarts J and Kes P H 1999 *Nature* **399** 665

[104] Sosolik C E, Stroscio J A, Stiles M D, Hudson E W,
     Blankenship S R, Fein A P and Celotta R J 2003 *Phys. Rev.*
     B **68** 140503
[105] Fischer Ø, Kugler M, Maggio-Aprile I, Berthod C and
     Renner Ch 2007 *Rev. Mod. Phys.* **79** 353
[106] Gammel P L, Bishop D J, Dolan G J, Kwo J R, Murray C A,
     Schneemeyer L F and Waszczk J 1987 *Phys. Rev. Lett.*
     59 2592
[107] Bolle C, Gammel P L, Grier D G, Murray C A, Bishop D J,
     Mitzi D B and Kapitulnik A 1991 *Phys. Rev. Lett.* **66** 112
[108] Grigorieva I V 1994 *Supercond. Sci. Technol.* **7** 161
[109] Marchevsky M, Keurentjes A, Kes P H and Aarts J 1997
     Physica C **282–287** 2085
[110] Pardo F, de la Cruz F, Gammel P L, Oglesby C S, Bucher E,
     Batlogg B and Bishop D J 1998 *Nature* **396** 348
[111] Vinnikov L Ya, Barkov T L, Canfield P C, Bud'ko S L and
     Kogan V G 2001 *Phys. Rev.* B **64** 024504
[112] Harada K, Matsuda T, Bonevich J, Igarashi M, Kondo S,
     Pozzi G, Kawabe U and Tonomura A 1992 *Nature* **360** 51
[113] Moser A, Hug H J, Parashikov I, Stiefel B, Fritz O,
     Thomas H, Baratoff A, Güntherodt H-J and
     Chaudhari P 1995 *Phys. Rev. Lett.* **74** 1847
[114] Roseman M and Grütter P 2001 *New J. Phys.* **3** 24.1
[115] Volodin A, Temst K, Van Haesendonck C, Bruynseraede Y,
     Montero M I and Schuller I K 2002 *Europhys. Lett.*
     58 582
[116] Schwarz A, Pi U H, Liebmann M, Wiesendanger R, Khim Z G
     and Kim D H 2006 *Appl. Phys. Lett.* **88** 012507
[117] Kirtley J R, Tsuei C C, Rupp M, Sun J Z, Yu-Jahnes L S,
     Gupta A, Ketchen M B, Moler K A and Bhushan M 1996
     Phys. Rev. Lett. **76** 1336
[118] Tsuei C C and Kirtley J R 2000 *Rev. Mod. Phys.* **72** 969
[119] Zhao X *et al* 2001 *Supercond. Sci. Technol.* **14** 1124
[120] Wynn J C, Bonn D A, Gardner B W, Lin Y-J, Liang R,
     Hardy W N, Kirtley J R and Moler K A 2001 *Phys. Rev.*
     Lett. **87** 197002
[121] Gardner B W, Wynn J C, Bonn D A, Liang R, Hardy W N,
     Kirtley J R, Kogan V G and Moler K A 2002 *Appl. Phys.*
     Lett. **80** 1010
[122] Plourde B L T, Van Harlingen D J, Saha N, Besseling R,
     Hesselberth M B S and Kes P H 2002 *Phys. Rev.* B
     66 054529
[123] Veauvy C, Hasselbach K and Mailly D 2002 *Rev. Sci. Instrum.*
     73 3825
[124] Kadowaki K 2005 *Sci. Tech. Adv. Mater.* **6** 589
[125] Oral A, Bending S J, Humphreys R G and Henini M 1997
     Supercond. Sci. Technol. **10** 17
[126] Grigorenko A N, Bending S J, Tamegai T, Ooi S and
     Henini M 2001 *Nature* **414** 728
[127] Crisan A, Pross A, Cole D and Bending S 2004 *Physica* C
     408–410 555
[128] Bluhm H, Sebastian S E, Guikema J W, Fisher I R and
     Moler K A 2006 *Phys. Rev.* B **73** 014514
[129] Straub R, Keil S, Kleiner R and Koelle D 2001 *Appl. Phys.*
     Lett. **78** 3645
[130] Goa P E, Hauglin H, Baziljevich M, Il'Yashenko E,
     Gammel P L and Johansen T H 2001 *Supercond. Sci.*
     Technol. **14** 729
[131] Hug H J, Stiefel B, van Schendel P J A, Moser A,
     Martin S and Güntherodt H-J 1999 *Rev. Sci. Instrum.*
     70 3625
[132] Kirtley J R 2002 *Physica* C **368** 55
[133] Dolocan V O, Veauvy C, Servant F, Lejay P, Hasselbach K,
     Liu Y and Mailly D 2005 *Phys. Rev. Lett.* **95** 097004
[134] Kim P, Yao Z and Lieber C 1996 *Phys. Rev. Lett.* **77** 5118
[135] Marchevsky M, Gurevich L A, Kes P H and Aarts J 1995
     Phys. Rev. Lett. **75** 2400
[136] Marchevsky M, Aarts A, Kes P H and Indenbom M V 1997
     Phys. Rev. B **78** 531
[137] Marchevsky M, Aarts A and Kes P H 1999 *Phys. Rev.* B
     60 14601
[138] Bitter F 1931 *Phys. Rev.* **38** 1903
[139] Balashova B M and Sharvin Iu V 1957 *Sov. Phys—JETP* **4** 54
[140] Hutchinson R I, Lavin P A and Moon J R 1965 *J. Sci. Instrum.*
     42 885
[141] Huebener R P 1979 *Magnetic Flux Structures in*
     Superconductors (Berlin: Springer)
[142] Weiss F, Sénatueur J P, Rounault A, Audier M, Bréchet Y,
     Blais S and Blum R 1993 *Cryogenics* **33** 50
[143] Kimoto K, Kamiya Y, Nonoyama M and Uyeda R 1963
     Japan. J. Appl. Phys. **2** 702
[144] Tasaki A, Tomiyama S, Iida S, Wada N and Uyeda R 1965
     Japan. J. Appl. Phys. **4** 707
[145] Gong W, Li H, Zhao Z and Chen J 1991 *J. Appl. Phys.*
     69 5119
[146] Sarma N V and Moon J R 1967 *Phil. Mag.* **16** 433
[147] Fournet G 1965 *Phys. Lett.* **17** 210
[148] Milleron P F, Fournet G and Franzinetti M 1971 *J. Low Temp.*
     Phys. **4** 545
[149] Fritz O, Wülfert M, Hug H J, Thomas H and Güntherodt H J
     1993 *Phys. Rev.* B **47** 384
[150] Kittel C 1949 *Rev. Mod. Phys.* **21** 541
[151] Fasano Y 2003 *PhD Thesis* Instituto Balseiro y Universidad
     Nacional de Cuyo, Bariloche
[152] Boaknin E, Hill R W, Proust C, Lupien C, Taillefer L and
     Canfield P C 2001 *Phys. Rev. Lett.* **87** 237001
[153] Pardo F 1997 *PhD Thesis* Instituto Balseiro y Universidad
     Nacional de Cuyo, Bariloche
[154] Gammel P L, Bishop D J, Rice J P and Ginsberg D M 1992
     Phys. Rev. Lett. **68** 3343
[155] Marchevsky M, Kes P H and Aarts J 1997 *Physica* C
     282–287 2083
[156] Banerjee S S *et al* 1998 *Phys. Rev.* B **58** 995
[157] Pearl J 1964 *Appl. Phys. Lett.* **5** 65
[158] Kogan V G, Yu Simonov A and Ledvij M 1993 *Phys. Rev.* B
     48 392
[159] Wei J and Yang T 1993 *Japan. J. Appl. Phys.* **35** 5696
[160] Henkels W H and Kircher C J 1977 *IEEE Trans. Magn.*
     13 63
[161] Nishio T 2008 unpublished
[162] Sugimoto A, Yamaguchi T and Iguchi I 1999 *J. Low Temp.*
     Phys. **117** 1347
[163] Yamada H, Moriai K, Kanno S, Aizawa K, Kusunoki M,
     Mukaida M and Ohshima S 2002 *Physica* C **378–381** 554
[164] Menghini M, unpublished
[165] Dai H, Liu J and Lieber C M 1994 *Phys. Rev. Lett.* **72** 748
[166] Halperin B I and Nelson D R 1978 *Phys. Rev. Lett.* **41** 121
[167] Montero M I *et al* 2002 *J. Phys. D: Appl. Phys.* **35** 2398
[168] Nelson D R and Halperin B I 1979 *Phys. Rev.* B **19** 2457
[169] Reichhardt C, Olson C J, Scalettar R T and Zimanyi G T 2001
     Phys. Rev. B **64** 144509
[170] Joseph T and Dasgupta Ch 2002 *Physica* B **66** 212506
[171] de Gennes P G 1976 *Superconductivity of Metals and Alloys*
     (New York: Addison-Wesley)
[172] Toledano P and Dimitriev V 1996 *Reconstructive Phase*
     Transitions (Singapore: World Scientific)
[173] Hatch D M, Lookman T, Saxena A and Stokes H T 2001
     Phys. Rev. B **64** 060104
[174] Cornaglia P S and Laguna M F 2003 *Phys. Rev.* B **67** 132503
[175] Laguna M F, Cornaglia P S and Aligia A A 2004 *Phys. Rev.* B
     69 104524
[176] Glazman L I and Koshelev A E 1991 *Phys. Rev.* B **43** 2835
[177] Daemen L L, Bulaevskii L N, Maley M P and Coulter J Y
     1993 *Phys. Rev.* B **47** 11291
[178] Kes P H, Aarts J, Vinokur V M and van der Beek C J 1990
     Phys. Rev. Lett. **64** 1063
[179] de la Cruz F, Fasano Y, de Seta M, Menghini M and
     Pastoriza H 2004 *J. Low Temp. Phys.* **99** 99

[180] Duarte A, Fernández Righi E, Bolle C A, de la Cruz F,
Gammel P L, Oglesby C S, Bucher E, Batlogg B and
Bishop D J 1996 *Phys. Rev.* B **53** 11336
[181] Pardo F, de la Cruz F, Gammel P L, Oglesby C S, Bucher E,
Batlogg B and Bishop D J 1997 *Phys. Rev. Lett.* **78** 4633
[182] Koshelev A E and Vinokur V M 1994 *Phys. Rev. Lett.*
73 3580

[183] Bending S J, Kaya I I, Ooi S, Tamegai T, Oral A, Barnard J C
and Henini M 1998 *Phys. Rev. Lett.* **80** 3610
[184] Soibel A, Zeldov E, Rappaport M, Myasoedov Y, Tamegai T,
Ooi S, Konczykowski M and Geshkenbein V B 2000
Nature **406** 282
[185] Tonomura A *et al* 2002 *Physica* C **369** 68
[186] Tonomura A 2003 *Physica* C **388** 624